Key Points:

- (De)hydration fronts propagate into zero-permeability rock if the solid density of the reactant is smaller than the one of the product
- External fluid flux compensates the imbalance between fluid generated/consumed by reaction and fluid needed to fill generated porosity
- Results of systematic numerical simulations allow estimating the transient, reaction-induced permeability of natural (de)hydration zones

Correspondence to:
S. M. Schmalholz,
stefan.schmalholz@unil.ch

(De)hydration Front Propagation Into Zero-Permeability Rock

Stefan M. Schmalholz[1] [ORCID]**, Lyudmila Khakimova**[1]**, Yury Podladchikov**[1] [ORCID]**, Erwan Bras**[2]**, Philippe Yamato**[2]**, and Timm John**[3] [ORCID]

[1]Institute of Earth Sciences, University of Lausanne, Lausanne, Switzerland, [2]CNRS, Géosciences Rennes UMR 6118, Université de Rennes, Rennes, France, [3]Institute of Geological Sciences, Freie Universität Berlin, Berlin, Germany

Abstract Hydration and dehydration reactions play pivotal roles in plate tectonics and the deep water cycle, yet many facets of (de)hydration reactions remain unclear. Here, we study (de)hydration reactions where associated solid density changes are predominantly balanced by porosity changes, with solid rock deformation playing a minor role. We propose a hypothesis for three scenarios of (de)hydration front propagation and test it using one-dimensional hydro-mechanical-chemical models. Our models couple porous fluid flow, solid rock volumetric deformation, and (de)hydration reactions described by equilibrium thermodynamics. We couple our transport model with reactions through fluid pressure: the fluid pressure gradient governs porous flow and the fluid pressure magnitude controls the reaction boundary. Our model validates the hypothesized scenarios and shows that the change in solid density across the reaction boundary, from lower to higher pressure, dictates whether hydration or dehydration fronts propagate: decreasing solid density causes dehydration front propagation in the direction opposite to fluid flow while increasing solid density enables both hydration and dehydration front propagation in the same direction as fluid flow. Our models demonstrate that reactions can drive the propagation of (de)hydration fronts, characterized by sharp porosity fronts, into a viscous medium with zero porosity and permeability; such propagation is impossible without reactions, as porosity fronts become trapped. We apply our model to serpentinite dehydration reactions with positive and negative Clapeyron slopes and granulite hydration (eclogitization). We use the results of systematic numerical simulations to derive a new equation that allows estimating the transient, reaction-induced permeability of natural (de)hydration zones.

Plain Language Summary We investigate reactions of hydration, which is the incorporation of water into a rock, and dehydration, which is the liberation of water from a rock, with simple mathematical models. These reactions are critical in understanding processes like plate tectonics, but many aspects of how hydration or dehydration fronts move through a rock are unclear. Our research focuses on reactions where changes in density are mostly balanced by changes in pore space, termed porosity, rather than the deformation of the solid rock. We developed mathematical models that combine fluid flow, rock deformation, and hydration/dehydration reactions. We derived simple equations that predict changes in porosity during hydration and dehydration, even when the solid rock deforms simultaneously. We found that whether a rock hydrates or dehydrates depends on how its solid density changes with increasing pressure during the reaction. By systematically studying our model, we discovered that the speed of hydration and dehydration is not influenced by the interval of fluid pressure over which the reaction occurs or the relationship between porosity and permeability. We present an equation that can be used to estimate permeability from natural (de)hydration zones.

1. Introduction

Hydration and dehydration reactions play a fundamental role in the evolution and dynamics of the solid Earth as well as in the evolution of life or modern industry (e.g., Ague, 2014; Ohtani, 2021; Putnis, 2021; Vitale Brovarone et al., 2020). Generally, hydration is a chemical reaction where a substance incorporates water and dehydration is a chemical reaction where a substance liberates water (e.g., Philpotts & Ague, 2022). We focus here on metamorphic reactions and use the term (de)hydration to refer to both hydration and dehydration reactions. In solid Earth sciences, the term water is often used as an analogy to fluid and mostly includes not only molecular H_2O but also OH groups or hydrogen, H (e.g., Kaatz et al., 2022; Vitale Brovarone et al., 2020). Furthermore, minerals can incorporate water in various ways during hydration, such as in hydrous minerals, nominally anhydrous minerals, or fluid inclusions (e.g., Kaatz et al., 2022; Liu et al., 2022; Putnis & John, 2010).
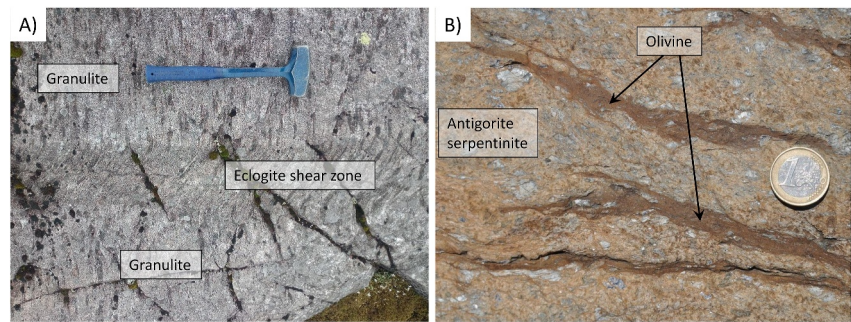
Figure 1. Photographs of natural rocks showing (a) hydration and (b) dehydration features. (a) Eclogite shear zone with eclogitization associated to deformation from Holsnøy, western Norway (60°35'11''N, 5°07'34''E). (b) Metamorphic olivine veins in antigorite serpentinite from the Erro Tobbio ultramafic rocks, Ligurian Alps, Italy (44°33'38.9''N, 8° 48'49.5''E).

(De)hydration is essential for the water and volatile cycle at subduction zones (e.g., Peacock, 1990; Plümper et al., 2017; Scambelluri et al., 2019). Furthermore, (de)hydration plays a pivotal role in many geodynamic processes because it changes the physical properties of rocks, for example, the density and associated buoyancy, the porosity and associated permeability, the melting temperature, or the effective viscosity (e.g., Karato, 2008; Ohtani, 2021; Putnis & John, 2010). Therefore, dehydration can change, for example, the stress state of rocks and trigger earthquakes (e.g., Ferrand et al., 2017) or the migration of liberated water can change the rock melting temperature and cause flux melting (e.g., Grove et al., 2006). Hydration also has a catalytic effect on metamorphic reactions (e.g., Putnis, 2021) and can significantly weaken rocks, potentially causing strain localization (e.g., Baïsset et al., 2024; Griggs & Blacic, 1965; Stünitz et al., 2017). Hence, most of the geodynamic importance of (de)hydration does not originate from the chemical reactions alone, but from coupling (de)hydration with porosity and density change, fluid flow, rock deformation, and associated stress changes.

Many studies have applied laboratory experiments with a variety of rocks to study hydration (e.g., Kuleci et al., 2016, 2017; Malvoisin et al., 2012; Zheng et al., 2019) and dehydration reactions (e.g., Brantut et al., 2012; Heard & Rubey, 1966; Jung et al., 2004; Leclère et al., 2018; Llana-Fúnez et al., 2012; Marti et al., 2021; Schrank et al., 2021). These experiments provide essential insight into the fundamental processes of (de)hydration. Many experiments are conducted on rocks such as gypsum which aim to mimic processes relevant to conditions in the Earth's upper crust or for deformation rates that are orders of magnitude faster than rates typical for slower, ductile geodynamic deformation processes. In addition to conducting experiments, it is necessary to develop mathematical models to understand the coupling of the physical and chemical mechanisms governing (de)hydration. Such models should be able to reproduce and predict laboratory experiments and allow studying (de)hydration under geodynamic conditions that are not feasible to achieve in laboratory experiments, such as slow deformation rates, say $<10^{-7}$ s^{-1}. The mathematical models are further well suited to determine the parameters and conditions that control the propagation and shape of reaction fronts in rock (e.g., Ague, 2014; Baumgartner & Ferry, 1991; Bickle & McKenzie, 1987; Fletcher & Hofmann, 1974; Koehn et al., 2021).

Rocks such as granulite and serpentinites (hydrated metaperidotites) are representative of the lower crust and hydrated lithospheric mantle, respectively. These rocks constitute an important part of the lithosphere and can be involved in (de)hydration processes that occur in deeper geodynamic settings below the upper crust. For example, the hydration of granulite can produce eclogite at high-pressure conditions (e.g., Austrheim, 1987) and the dehydration of antigorite serpentinite can produce olivine and liberate fluids during subduction (e.g., Ulmer & Trommsdorff, 1995). Well-studied field examples of these two reactions are presented in Figure 1. There have been many investigations on (de)hydration processes, either from a chemical perspective focusing on fluid and mineral chemistry and thermodynamic phase calculations, while disregarding hydro-mechanical flow and deformation processes (e.g., Centrella et al., 2015; Massonne, 2009), or from a hydro-mechanical perspective focusing on poromechanical models, while often neglecting chemical aspects and their impact on changes in porosity, density, and fluid pressure (e.g., Cagnioncle et al., 2007; Gerya & Meilick, 2011; Hu et al., 2022; Quinquis & Buiter, 2014). Such focus on either chemical (C) or hydro-mechanical (HM) processes is frequently reasonable because the investigated processes, and associated observations and experiments, are often quite complex. However, many aspects of (de)hydration remain unclear, such as the hydration of rock in the limit of

zero-permeability, or zero connected porosity, the generation of transient, reaction-induced permeability during simultaneous (de)hydration and deformation, or the parameters and conditions controlling the propagation of (de)hydration fronts. Important geological examples where these relationships are certainly of importance are the hydration of high-pressure rocks during subduction and exhumation, such as the eclogitization of lower crustal granulites by fluid migration through shear zones (e.g., Austrheim, 1987; our Figure 1a), or the dehydration of deforming antigorite serpentinite and the associated formation of olivine veins during subduction (e.g., Hermann et al., 2000; our Figure 1b). Hence, an increasing number of mathematical studies apply models that consider the hydro-mechanical-chemical (HMC) coupling of reactions, fluid flow, and deformation to address some of the unclear aspects mentioned above (e.g., Bras et al., 2023; O. Evans et al., 2018, 2020; Keller & Suckale, 2019; Malvoisin et al., 2015, 2021; Poulet et al., 2014; Schmalholz et al., 2020, 2023).

The main aim of our study is to mathematically investigate fundamental aspects of coupled HMC processes related to (de)hydration, including the quantification of porosity change, and the parameters controlling the propagation of (de)hydration fronts. We apply simple, but representative, models to simplify the mathematical treatment and ensure transparency. We consider elastic or viscous volumetric deformation for the M-models and Darcy flow for the H-models. For the C-models, we concentrate on a specific group of (de)hydration reactions: (de)hydration reactions whose density changes can be mainly balanced by porosity changes. The considered (de)hydration generates reaction-induced porosity and permeability. The solid volumetric deformation associated with the considered (de)hydration plays a minor role. Furthermore, we consider only pure H_2O as the free fluid phase. The modeled system can be open or closed concerning H_2O but is closed concerning the solid components such as MgO or SiO_2. We further assume that the dissolution of solid components into the fluid phase has a negligible contribution to the overall mass balance. An example of a dehydration reaction compatible with the features mentioned above is the dehydration of serpentinite, made of antigorite and brucite, into forsterite and pure H_2O (e.g., B. W. Evans, 2004; our Figure 1b). An example of a hydration reaction compatible with the features mentioned above is the hydration of felsic granulite into eclogite (e.g., Bras et al., 2023; our Figure 1a). Furthermore, estimates of porosity relevant for metamorphism in deeper rock range between 10^{-3} and 10^{-6} (e.g., Ague, 2014; Kaatz et al., 2023; Skelton, 2011) and estimates for permeability are as low as 10^{-23} m^2 (e.g., Ague, 2014; Katayama et al., 2012) or even lower when extrapolated to confining pressures >10 kbar (e.g., Hatakayama et al., 2017). Therefore, we consider the endmember scenario of a rock with zero porosity and zero permeability, representing conditions for which Darcy flow is geologically irrelevant. The applied simplifications keep our mathematical models as simple as possible but as complex as necessary to capture the essential features of the propagation of (de)hydration fronts in rock.

For the considered conditions of (de)hydration mentioned above, we formulate a hypothesis that explains why for some metamorphic reactions involving a free fluid phase either a hydration or dehydration front can propagate and into which direction. In equilibrium thermodynamics and for isothermal conditions the pressure controls the reaction boundary (Figures 2a and 2c). For (de)hydration reactions, the porosity can be generated on either the high-pressure or low-pressure side of the reaction boundary. We propose that this porosity-pressure relation controls the type of the reaction, either hydration or dehydration, and its propagation direction. We elaborate our hypothesis in more detail in Section 2 and we test our hypothesis with one-dimensional (1D) mathematical HMC models. These HMC models are based on the general concepts of continuum mechanics and classical irreversible thermodynamics (e.g., Lebon et al., 2008; Malvern, 1969) which are commonly applied to quantify geodynamic and metamorphic processes (e.g., Philpotts & Ague, 2022; Turcotte & Schubert, 2014). We aim to transparently present the mathematical models to address a broad scientific community, ranging from petrology to geophysics. In addition to testing our hypothesis for (de)hydration, we will (a) explain the mechanism of (de)hydration front propagation in the limit of zero permeability, (b) present a quantification for reaction-induced porosity generation during (de)hydration involving volumetric rock deformation, (c) show a systematic analysis of (de)hydration involving the quantification of the velocity of (de)hydration front propagation, (d) apply our results to estimate reaction-induced permeabilities for published case studies of (de)hydrated rock and (e) provide a 1D numerical algorithm for (de)hydration front propagation into zero-permeability rock.

2. The Hypothesis for (De)hydration Front Propagation

We investigate the following scientific question: How can a reactive (de)hydration front invade an initially zero-porosity, impermeable rock, and what are the governing parameters? We hypothesize that the propagation of (de)hydration fronts into an initially zero-porosity rock is primarily governed by the particular combination of (a)
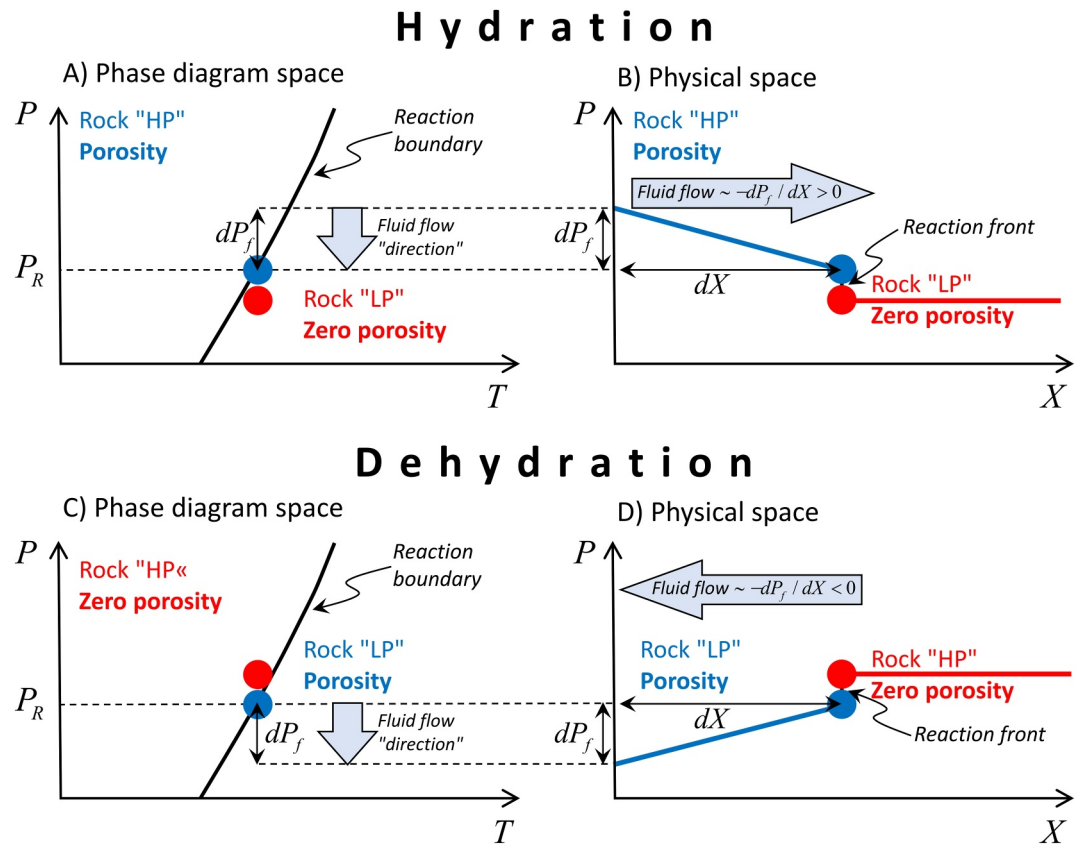
Figure 2. Schematic diagrams showing the proposed hypothesis for hydration (panels a and b) and dehydration (c and d) scenarios. Panels (a) and (c) show the respective scenarios in the pressure, *P*, versus temperature, *T*, diagram (like in a typical *P-T* phase diagram) and (b) and (d) in the physical space, that is pressure versus distance, *X*. Fluid can only flow in rock with porosity and permeability (blue color) and this flow always occurs from high to low fluid pressure (light blue arrow). There is no free fluid, and, hence no fluid pressure and no fluid flow in a zero-porosity, impermeable rock (red color).

the fluid pressure gradient around the reaction front and (b) the change in solid density during the reaction, inducing a porosity generation. We consider here spatial scales much larger than the individual pore size so that we can test our hypothesis with mathematical models based on continuum-poromechanics concepts (e.g., Coussy, 2004; see also Section 3.1), which necessarily implies ignoring processes acting on the pore scale and smaller. In the subsequent paragraphs, we elaborate on our hypothesis.

Our hypothesis involves reaction-induced porosity generation. For a closed system without fluid flow and dissolution, the porosity generated by a reaction can be calculated with the associated molar volume change of the total solid and fluid of the system under consideration (e.g., Putnis, 2009). For an open system with fluid flow, we suggest that the porosity generation by reaction front propagation involving fluid flow can be explained by coupling chemical models based on equilibrium thermodynamics (Figures 2a and 2c) with Darcy-type hydraulic transport models (Figures 2b and 2d). We propose coupling the two models through the fluid pressure: the fluid pressure controls the thermodynamic pressure magnitude applied in the thermodynamic equilibrium calculations and the fluid pressure gradient governs fluid flow (Figure 2).

We consider hydration and dehydration reactions (Figure 2). We assume isothermal conditions so that the reactions are controlled by pressure only. Porosity can be generated by a reaction either on the high- or low-pressure side of the reaction (Figures 2a and 2c). The magnitude of the generated porosity is governed by the change in solid density and mass fraction of H$_2$O structurally bound in the solid. We propose that the porosity-pressure relation is essential for different scenarios of porosity generation by reaction front propagation.

We consider an initial, static rock in the limit of zero porosity in which (de)hydration front propagation will generate a transient porosity and permeability increase. For hydration reactions, the externally derived fluid must

always flow toward the initially zero-permeability rock and the hydration front propagates in the same direction as the fluid inflow; the scenario we term here hydration (Figures 2a and 2b). For dehydration reactions, there are two possible scenarios: In the first scenario, the liberated fluid flows away from the dehydrating rock in the direction opposite to the dehydration front propagation; the scenario we term here dehydration (Figures 2c and 2d). In the second scenario, the generated porosity due to dehydration is so large that the liberated fluid cannot fill the generated porosity, and externally derived fluid flows in the same direction as the dehydration front propagation to fill the generated pore space; the scenario we term here dehydration-inflow. We test the three hypothesized scenarios with mathematical models described in the next section.
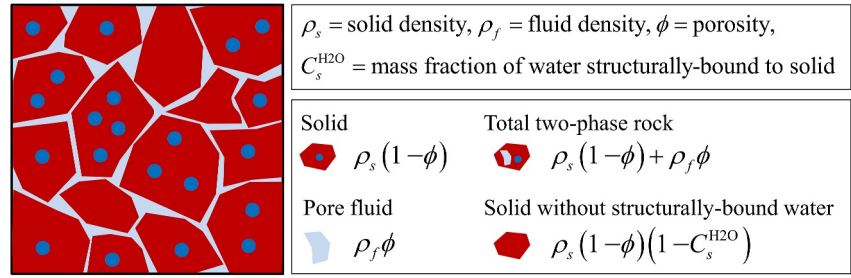
3. Mathematical Model

3.1. Overview and Structure

Before introducing the governing equations of the applied mathematical models, we provide a brief background for the applied theoretical concepts and an overview of the applied models. We consider for the individual mechanical (M), hydraulic (H), and chemical (C) processes simple, but representative, models: elastic or viscous volumetric deformation for M-models, Darcy flow for H-models and thermodynamic equilibrium reactions for the C-models. To construct our coupled mathematical HMC models, we employ the theoretical concepts of continuum mechanics (e.g., Hobbs & Ord, 2015; Malvern, 1969; Mase, 1970), poromechanics (e.g., Biot, 1941, 1962; Coussy, 2004) and classical irreversible thermodynamics (e.g., De Groot & Mazur, 1984; Kuiken, 1994; Lebon et al., 2008; Müller, 2007). Classical irreversible thermodynamics employs the so-called local equilibrium hypothesis. Thereby it is assumed that equilibrium, formulated by Gibbs' specific fundamental equation, applies locally although the overall process under investigation is dissipative, hence irreversible, due to, for example, the occurrence of heat conduction or viscous flow (e.g., Gibbs, 1906; Kuiken, 1994; Moulas et al., 2019). There are no differences or gradients in chemical potential for the applied local equilibrium thermodynamics. In equilibrium thermodynamics and for a given composition and isothermal conditions considered here, metamorphic reactions are controlled by the thermodynamic pressure. We assume that the magnitude of the thermodynamic pressure is equal to the magnitude of the fluid pressure, an assumption that is supported by theoretical considerations (e.g., Dahlen, 1992; Sekerka & Cahn, 2004), laboratory dehydration experiments (Llana-Fúnez et al., 2012) and molecular dynamics simulations (e.g., Frolov & Mishin, 2010; Mazzucchelli et al., 2024; see also Appendix C).

In continuum mechanics, the fundamental equations are typically partial differential equations (PDEs) which describe the conservation of certain quantities, such as mass. Constitutive equations describe the deformation behavior of the considered medium, such as viscous flow. In typical continuum mechanics applications, usually one phase only is considered, for example, the deformation of a solid or the flow of a fluid. In poromechanics, a porous solid phase is typically considered together with a fluid phase. Thereby, the solid and fluid phases are not spatially separated, instead, the differential equations describing solid and fluid motion are spatially superimposed. Hence, there is a solid and a fluid velocity at the same location in the mathematical model for a porous rock. We apply such two-phase model consisting of a solid phase with associated solid velocity and a fluid phase with a fluid velocity. We describe porous fluid flow by the well-established Darcy's law which was first derived empirically based on experiments (Darcy, 1856) and was later derived theoretically with averaging procedures applied to the continuum mechanics equations (e.g., Gray & O'Neill, 1976; Pride & Berryman, 1998; Whitaker, 1969, 1986; Yarushina & Podladchikov, 2015).

For simplicity and transparency, we focus here on 1D models only. We first present 1D HM models without (de)hydration reaction and restrict the volumetric deformation to poroelasticity. We consider linear and nonlinear porosity-permeability relations for which the permeability depends on some power of the porosity. We perform these 1D HM models to investigate porous flow in the zero-permeability limit. Such a zero-permeability limit can be envisaged for example, as dense crystalline rocks at high pressure and temperature conditions where porosities can be as low as 10^{-4}, and in some cases maybe even lower, so that the pores are not well connected and the permeability is essentially zero (e.g., Kaatz et al., 2022; Katayama et al., 2012; Taetz et al., 2018). Next, we present 1D HC models with (de)hydration but without solid deformation. Then, we present 1D HMC models with (de)hydration and viscous volumetric deformation of the solid. We apply these HC and HMC models to study the fundamental aspects of the coupling between (de)hydration, fluid flow, and porosity generation, particularly the propagation of (de)hydration fronts. Finally, we describe the applied thermodynamic calculations and the considered reactions. The H(M)C models with (de)hydration are derived with a mass-based formulation and

Figure 3. Simplified representation of a porous rock with an explanation of the partial densities applied in the mathematical models. Red areas represent the solid, light blue areas the pore fluid, and dark blue circles the structurally bound water in the solid. All symbols are explained in Table 1.

involve mass fractions and densities. A main result of these models is the derivation of analytical formulas that quantify porosity change during (de)hydration. To show the consistency of our results, we also derive these formulas for porosity change with a molar-based approach (Appendix B). Finally, we describe the applied numerical method to solve the presented H(M)C models.

3.2. Hydro-Mechanical Model I: Linear Diffusion Equation for Fluid Pressure and Porosity

We consider a 1D porous medium representing a solid-fluid mixture. We first ignore reactions. We start with the equation for the conservation of fluid mass per unit volume which is in the absence of reactions and chemical-diffusive fluxes given by

$$\frac{\partial}{\partial t}\left(\phi \rho_f\right) = -\frac{\partial}{\partial x}\left(v_f \phi \rho_f\right),$$
(1)

with t being the time, ϕ the porosity, ρ_f the fluid density, v_f the fluid velocity and x the spatial coordinate (Figure 3). Symbols used in the text are explained in Table 1. Equation 1 represents one equation for three unknowns, namely, ϕ, ρ_f, and v_f. To transform Equation 1 into a linear diffusion equation for the fluid pressure, P_f, we assume that ρ_f is constant, apply Darcy's law and the equation of state for elastic pore compressibility. Darcy's law for a constant permeability, k, and in the absence of gravity is

$$\phi v_f = -\frac{k}{\eta_f}\frac{\partial P_f}{dx},$$
(2)

with η_f being the fluid viscosity. We ignore gravity for simplicity, but the absence of gravity could be interpreted as considering only fluid pressure gradients orthogonal to the direction of gravity. The effects of pore compressibility in classical poroelasticity (e.g., Biot & Willis, 1957; Kümpel, 1991) can be expressed by the equation (Yarushina & Podladchikov, 2015, their Equation 22)

$$\frac{\partial \phi}{\partial t} = -\beta_\phi \frac{\partial P_f}{\partial t},$$
(3)

with β_ϕ being the constant elastic pore compressibility. Equation 3 can be integrated in time to yield

$$\phi = \phi_0 + \beta_\phi\left(P_f - P_{f0}\right),$$
(4)

with ϕ_0 and P_{f0} being the initial porosity and fluid pressure, respectively. Substituting Equations 2 and 4 into Equation 1 and assuming that ρ_f is a constant yields

$$\frac{\partial P_f}{\partial t} = \frac{\partial}{\partial x}\left(\frac{k}{\beta_\phi \eta_f}\frac{\partial P_f}{dx}\right).$$
(5)

Table 1
Symbols Used in the Text

Symbol	Name/definition	Units
x	Spatial coordinates	(m)
L_c	Characteristic length	(m)
k, k_0	Permeability, initial permeability	(m^2)
k_{ref}	Reference permeability, constant	(m^2)
k_c	Characteristic hydraulic parameter	(m^2 Pa^{-1} s^{-1})
V, V_0	Volume, initial volume	(m^3)
t	Time	(s)
t_c	Characteristic time	(s)
v_s	Solid velocity	(m s^{-1})
v_f	Fluid velocity	(m s^{-1})
v_c	Characteristic velocity	(m s^{-1})
v_F	Velocity of (de)hydration front	(m s^{-1})
P_f	Fluid pressure	(Pa)
P	Total pressure	(Pa)
P_R	Reaction pressure	(Pa)
P_c	Characteristic pressure	(Pa)
ΔP_f	Fluid pressure interval	(Pa)
β_ϕ	Pore compressibility	(Pa^{-1})
β_s	Solid compressibility	(Pa^{-1})
β_f	Fluid compressibility	(Pa^{-1})
η_f	Fluid viscosity	(Pa s)
η_ϕ	Compaction viscosity	(Pa s)
ρ_s, ρ_{s0}	Solid density, initial solid density	(kg m^{-3})
ρ_f, ρ_{f0}	Fluid density, initial fluid density	(kg m^{-3})
ρ_T	Total density	(kg m^{-3})
ρ_{im}	Density of immobile solid; $\rho_s\left(1 - C_s^{\text{H}_2\text{O}}\right)$	(kg m^{-3})
$\Delta\rho_s^R$	Solid density change across reaction	(kg m^{-3})
$M_{...}^{\text{mol}}$	Molar mass of component	(g mol^{-1})
$\tilde{P}_f$	Dimensionless fluid pressure	()
$\tilde{v}_f$	Dimensionless fluid velocity	()
$\phi, \phi_0, \phi_{\text{ref}}$	Porosity, initial and reference porosity	()
$\Delta\phi^R$	Porosity change across reaction	()
n	Exponent in the ϕ versus k relation	()
$C_s^{\text{H}_2\text{O}}$	Mass fraction of H$_2$O in solid	()

Equation 5 represents a linear diffusion equation for P_f. The parameter $k/(\beta_\phi\eta_f)$ has units of m^2/s and plays the role of an effective diffusion coefficient, often termed hydraulic diffusivity. Substituting Equation 4 into Equation 5 and, for simplicity setting $\phi_0 = 0$ and $P_{f0} = 0$, results in a linear diffusion equation for ϕ:

$$\frac{\partial\phi}{\partial t} = \frac{\partial}{\partial x}\left(\frac{k}{\beta_\phi\eta_f}\frac{\partial\phi}{dx}\right). \tag{6}$$

In the derivation above, the consideration of poroelasticity, here expressed by Equations 3 and 4, is essential to derive a diffusion-type equation for ϕ. The final equations for ϕ and P_f are diffusion-type equations, but have been derived from a mass balance equation including an advective flux of fluid mass, $v_f\phi\rho_f$, in Equation 1. The main characteristics of the model are summarized in Table 2.

3.3. Hydro-Mechanical Model II: Nonlinear Diffusion Equation for Fluid Pressure and Porosity

We consider now that the permeability is a function of the porosity by applying a nonlinear permeability-porosity relationship, similar to a Kozeny-Carman formulation (e.g., Carman, 1937; Coussy, 2004; Kozeny, 1927), of the form

$$k = k_{\text{ref}}\left(\frac{\phi}{\phi_{\text{ref}}}\right)^n, \tag{7}$$

with k_{ref} being a reference permeability, ϕ_{ref} being a reference porosity and n being a power-law exponent controlling the nonlinearity between k and ϕ. The permeability of highly nonlinear or fractured rocks can be reproduced using a large power-law exponent and, in this case, this relation can be interpreted as a linear approximation of the experimentally measured dependence of permeability on porosity in logarithmic coordinates (e.g., Yarushina et al., 2021). For simplicity, we set again $\phi_0 = 0$ and $P_{f0} = 0$ in the poroelastic Equation 4 so that substituting Equations 4 and 7 into Equation 5 yields

$$\frac{\partial P_f}{\partial t} = \frac{1}{\beta_\phi}\frac{\partial}{\partial x}\left(\frac{k_{\text{ref}}}{\eta_f}\left(\frac{\beta_\phi P_f}{\phi_{\text{ref}}}\right)^n\frac{\partial P_f}{dx}\right), \tag{8}$$

which represents a nonlinear diffusion equation for the fluid pressure. Alternatively, Equation 8 can be reformulated as a nonlinear diffusion equation for ϕ. Substituting $P_f = \phi/\beta_\phi$ from Equation 4 into Equation 8 yields

$$\frac{\partial\phi}{\partial t} = \frac{\partial}{\partial x}\left(\frac{k_{\text{ref}}}{\beta_\phi\eta_f}\left(\frac{\phi}{\phi_{\text{ref}}}\right)^n\frac{\partial\phi}{dx}\right). \tag{9}$$

We perform representative numerical solutions of the above-described linear, Equation 6, and nonlinear, Equation 9, diffusion equations in the Results Section 4. Equation 9 is mathematically equivalent to thin-film equations resulting from lubrication theory and the equation for the shallow ice approximation used for glacier flow modeling (e.g., Huppert, 1982; Hutter, 2017; Mahaffy, 1976).

In the HM models I and II above, we consider only the elastic behavior of the porous matrix. We do not consider a viscous matrix behavior because it is well-established that in a poroviscous matrix, the propagation velocity of

Table 2
Overview of Models and Some of Their Characteristics

Model	Type	Dynamic permeability	Trapped at zero porosity limit	Sharp front	Efficient mass transport	Channel forming ability	Volumetric deformation
I	HM	No	Yes	No	No	No	Elastic
II	HM	Yes	No	Yes	No	No	Elastic
III	HC	Yes	No	Yes	Yes	No	None
IV	HMC	Yes	No	Yes	Yes	Yes	Viscous

Note. Under category "Type," H means that porous flow is considered, M that solid volumetric deformation is considered, and C that metamorphic reactions are considered.

pore fluid fronts vanishes with vanishing porosity, which means that in the most extreme case, pore fluids get trapped by a viscous matrix with zero porosity (e.g., Barcilon & Richter, 1986; Connolly & Podladchikov, 2015). For completeness, we provide the expression for the pore fluid propagation velocity, $v_{f\phi}$, in a poroviscous matrix with constant compaction viscosity:

$$v_{f\phi} = \left(\rho_s - \rho_f\right) g \frac{k_0}{\eta_f} \phi_0^{n-2}\left(2\phi_{\max} + \phi_0\right), \tag{10}$$

where k_0 is the permeability coefficient for the poroviscous matrix, ϕ_0 is the porosity of the poroviscous matrix and ϕ_{max} is the porosity of the pore fluid front that propagates through the poroviscous matrix. A pore fluid front can only be developed and propagate for $n > 2$ (e.g., Barcilon & Richter, 1986; Connolly & Podladchikov, 2015). Therefore, if $\phi_0 = 0$, then $v_{f\phi} = 0$ and the pore fluid front is trapped by a poroviscous matrix in the limit of zero porosity. We will show further below that pore fluid fronts can propagate into a poroviscous matrix with zero porosity and permeability if (de)hydration reactions are considered.

3.4. Hydro-Chemical Model III Involving (De)hydration Reactions

The (de)hydration significantly changes the solid density, ρ_s, and we, hence, consider now changes in ρ_s (Figure 3). Therefore, we employ the equation for the conservation of total mass per unit volume which for the absence of solid deformation (i.e., solid velocities are zero) and chemical-diffusive fluxes is

$$\frac{\partial \rho_T}{\partial t} = -\frac{\partial}{\partial x}\left(v_f \phi \rho_f\right), \tag{11}$$

where the total rock density $\rho_T = \rho_s(1 - \phi) + \rho_f \phi$ (Figure 3). For HC models with (de)hydration, we also need to consider that the amount of H_2O, which is structurally bound to the solid, changes during (de)hydration. Hence, we employ an additional equation for the conservation of the total mass of the solid without the mass of structurally bound H_2O in the solid:

$$\frac{\partial}{\partial t}\left(\rho_s(1 - \phi)\left(1 - C_s^{H_2O}\right)\right) = 0, \tag{12}$$

where $C_s^{H_2O}$ is the mass fraction of H_2O structurally bound in the solid (Figure 3). To illustrate the parameter $C_s^{H_2O}$, we consider brucite, that is $Mg(OH)_2$. Brucite has a molar mass, M_{Bru}^{mol}, of 58.32 g/mol and water has a molar mass, $M_{H_2O}^{mol}$, of 18.02 g/mol. The mass fraction of structurally bound water in brucite is $C_s^{H_2O} = M_{H_2O}^{mol}/M_{Bru}^{mol} = 18.02/58.32 \approx 0.31$. Because there is no solid deformation and we assume no chemical diffusion between solid and fluid, there are no mass fluxes and the total mass of solid without structurally bound H_2O is constant. Therefore, Equation 12 can be integrated in time to yield

$$\rho_s(1 - \phi)\left(1 - C_s^{H_2O}\right) = \rho_{s0}(1 - \phi_0)\left(1 - C_{s0}^{H_2O}\right), \tag{13}$$

where all parameters with subscript "0" indicate initial values determined by the initial total mass of solid without structurally bound H_2O. To study the zero-porosity limit, we assume that $\phi_0 = 0$ and solve Equation 13 for ϕ which yields (e.g., Malvoisin et al., 2015)

$$\phi = 1 - \frac{\rho_{s0}(1 - C_{s0}^{H_2O})}{\rho_s(1 - C_s^{H_2O})}. \tag{14}$$

We assume that the thermodynamic pressure in the equation for Gibbs free energy is quantified by P_f. The thermodynamic calculations are described further below (see Section 3.7). We apply thermodynamic phase calculations for a specific reaction and calculate values of densities and mass fraction for different values of P_f. Densities and mass fraction are, hence, a function of P_f. This dependence is expressed by

$$\begin{aligned} \rho_s &= \rho_s(P_f) \\ \rho_f &= \rho_f(P_f) \\ C_s^{H_2O} &= C_s^{H_2O}(P_f) \end{aligned} \tag{15}$$

Due to these dependencies of densities and mass fraction on P_f, ϕ from Equation 14 also indirectly depends on P_f and we can write

$$\phi = \phi(P_f). \tag{16}$$

We will provide explicit relations between ρ_s, ρ_f, $C_s^{H_2O}$, and P_f based on thermodynamic equilibrium calculations for specific reactions in the next section. Substituting Darcy's law, Equation 2, and a Kozeny-Carman permeability formulation, Equation 7, into the conservation Equation 11 for total mass yields

$$\frac{\partial \rho_T(P_f)}{\partial t} = \frac{\partial}{\partial x}\left(\rho_f(P_f) \frac{k_{\text{ref}}}{\eta_f}\left(\frac{\phi(P_f)}{\phi_{\text{ref}}}\right)^n \frac{\partial P_f}{dx}\right), \tag{17}$$

in which we indicated for clarity the dependencies of ρ_T, ρ_f, and ϕ on P_f.

3.5. Hydro-Mechanical-Chemical Model IV Involving (De)hydration Reactions and Viscous Solid Deformation

We elaborate the HC model presented above to an HMC model by considering the solid volumetric deformation. First, the solid deformation is added in the conservation equation for total mass, Equation 11, to yield (e.g., Schmalholz et al., 2020)

$$\frac{\partial \rho_T}{\partial t} = -\frac{\partial}{\partial x}\left((v_f - v_s)\phi\rho_f\right) - \frac{\partial}{\partial x}(v_s\rho_T), \tag{18}$$

where v_s is the velocity of the solid phase. The particular form of Equation 18 is derived in detail in Schmalholz et al. (2020). We assume a viscous solid volumetric deformation and the constitutive equation for this deformation can be written as

$$\frac{\partial}{\partial x}(v_s) = \frac{P_f - P}{\eta_\phi}, \tag{19}$$

where η_ϕ is the compaction viscosity (e.g., McKenzie, 1984) and P is the total pressure. For simplicity, we assume that P is a constant ambient pressure, for example, the lithostatic pressure, and that η_ϕ is constant. We use the solid strain rate, $\partial v_s/\partial x$, to calculate v_s by

$$v_s = \int_0^x \frac{\partial}{\partial x}(v_s)\, dx. \tag{20}$$

Second, solid deformation is added to the conservation equation for the solid without structurally bound water, Equation 12, to yield

$$\frac{\partial}{\partial t}\big(\rho_s(1-\phi)\big(1-C_s^{\mathrm{H_2O}}\big)\big) = -\frac{\partial}{\partial x}\big(v_s\rho_s(1-\phi)\big(1-C_s^{\mathrm{H_2O}}\big)\big). \tag{21}$$

The solid strain rate, $\partial v_s/\partial x$, can be related to a change in volume, V, via

$$\frac{\partial}{\partial x}(v_s) = \frac{1}{V}\frac{dV}{dt} = \frac{d}{dt}(\ln V). \tag{22}$$

Using Equation 22, the Equation 21 can be rearranged after some algebraic operations (Khakimova & Podladchikov, 2024; see also Appendix A) to

$$\frac{d}{dt}\big(\rho_s(1-\phi)\big(1-C_s^{\mathrm{H_2O}}\big)V\big) = 0. \tag{23}$$

Equation 23 can be integrated in time, such as Equation 12, to provide

$$\rho_s(1-\phi)\big(1-C_s^{\mathrm{H_2O}}\big)V = \rho_{s0}(1-\phi_0)\big(1-C_{s0}^{\mathrm{H_2O}}\big)V_0, \tag{24}$$

where V_0 is the initial volume. Assuming again $\phi_0 = 0$, ϕ is then given by Khakimova & Podladchikov (2024)

$$\phi = 1 - \frac{\rho_{s0}\big(1-C_{s0}^{\mathrm{H_2O}}\big)}{\rho_s\big(1-C_s^{\mathrm{H_2O}}\big)}\frac{V_0}{V}. \tag{25}$$

Equation 25 quantifies the change in ϕ caused by both (de)hydration and solid volumetric deformation.

3.6. Numerical Method and Model Configuration

We discretize the governing PDEs (6), (9) and (17) using the finite difference method on a 1D regular Cartesian grid (e.g., Patankar, 2018; Virieux, 1986). The linear and nonlinear diffusion Equations 6 and 9 without reactions are solved with a standard explicit time marching scheme (e.g., Patankar, 2018).

For the numerical solution of Equation 17 in combination with Equations 14 and 15, we apply the accelerated pseudo-transient (PT) method to solve the discretized Equation 17 for P_f in an iterative and matrix-free fashion (e.g., Chorin, 1997; Räss et al., 2022). We use a relaxation, or continuation, approach to handle the nonlinearities, such as ϕ-dependent permeability as well as P_f-dependent densities and ϕ, within the iterative procedure (e.g., Räss et al., 2019; Schmalholz et al., 2023; Wang et al., 2022). Upon convergence, these iterations provide results equivalent to results of a numerical-implicit method, since the gradients of the numerical variables are updated in each iteration.
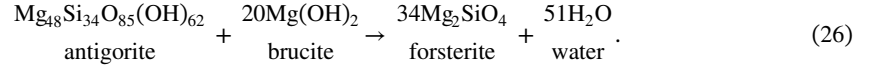
For solving the diffusion-type Equations 6 and 9 for ϕ, we apply as initial condition a Gaussian distribution of ϕ and keep the values of ϕ at the two model boundaries constant during the simulations, representing Dirichlet boundary conditions.

For solving Equation 17 for P_f, we apply initially constant values of P_f in the model except at one boundary where the value of P_f is either larger or smaller. The boundary values of P_f are also kept constant during the simulations. We provide more details on specific initial and boundary conditions when we present the results in the Results Section 4.

3.7. Thermodynamic Calculations

We consider local thermodynamic equilibrium and isothermal conditions to calculate the variation of ρ_s and ρ_f for varying P_f for specific reactions based on Gibbs free energy minimization. We apply the software Perple_X (e.g., Connolly, 2005) for the thermodynamic calculations based on Gibbs free energy minimization. The solid and fluid densities required for our calculations are thermodynamically constrained and we obtain them from the

thermodynamic calculations (e.g., Malvoisin et al., 2015). We consider two relatively simple representative reactions: (1) For dehydration, we consider a simple MSH system and the reaction: antigorite + brucite = forsterite + water at 500°C (e.g., B. W. Evans, 2004; Padrón-Navarta et al., 2013; Schmalholz et al., 2023). In the following, we refer to this reaction as the serpentinite to olivine reaction (SOR). This reaction represents the brucite-out reaction at which brucite breaks down, but antigorite can still be stable at higher temperatures and pressure (e.g., Plümper et al., 2017). The SOR is:

$$\underset{\text{antigorite}}{\text{Mg}_{48}\text{Si}_{34}\text{O}_{85}(\text{OH})_{62}} + \underset{\text{brucite}}{20\text{Mg}(\text{OH})_2} \rightarrow \underset{\text{forsterite}}{34\text{Mg}_2\text{SiO}_4} + \underset{\text{water}}{51\text{H}_2\text{O}}. \tag{26}$$

In a pressure-temperature phase diagram, the corresponding reaction boundary has a positive Clapeyron slope (e.g., Plümper et al., 2017). A similar dehydration reaction is the antigorite-out reaction occurring at higher temperatures: antigorite = forsterite + enstatite + water (e.g., Malvoisin et al., 2015; Ulmer & Trommsdorff, 1995). This antigorite-out reaction can occur for a positive Clapeyron slope at lower pressure and a negative Clapeyron slope at higher pressure (e.g., Malvoisin et al., 2015; Ulmer & Trommsdorff, 1995). We will focus on the brucite-out reaction, SOR, but also discuss the application of the results for the SOR to the antigorite-out reaction.

(2) For hydration, we consider the reaction: "felsic granulite" + water = "felsic eclogite" at 700°C (Bras et al., 2023). In the following, we refer to this reaction as the granulite to eclogite reaction (GER). The GER is:

$$\underset{\text{albite}}{4\text{Na}(\text{AlSi}_3\text{O}_8)} + \underset{\text{anorthite}}{4\text{Ca}(\text{Al}_2\text{Si}_2\text{O}_8)} + \underset{\text{water}}{\text{H}_2\text{O}} \rightarrow \underset{\text{jadeite}}{4\text{NaAl}(\text{Si}_2\text{O}_6)} + \underset{\text{kyanite}}{\text{Al}_2\text{SiO}_5} + \underset{\text{zoesite}}{2\text{Ca}_2\text{Al}_3(\text{SiO}_4)_3(\text{OH})} + \underset{\text{quartz}}{5\text{SiO}_2}. \tag{27}$$
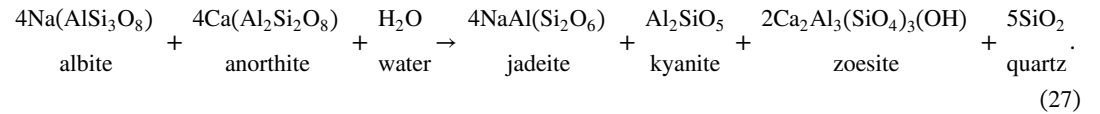
In the GER, the "granulite" represents a granulite facies rock consisting of plagioclase only and "eclogite" represents consequently a felsic eclogite facies rock (e.g., Bras et al., 2023; Wayte et al., 1989).

For both reactions, the thermodynamic calculations will provide the values of ρ_s and ρ_f as function of P which we present in more detail in the Result Section 4. For the isothermal conditions and for simple univariant reactions, the reaction occurs at a specific value of P which we term the reaction pressure P_R. The values of $C_s^{\text{H}_2\text{O}}$ for each side of the reaction can be calculated from the molar masses of the involved elements and minerals (e.g., Bras et al., 2023; Schmalholz et al., 2023). The values of $C_s^{\text{H}_2\text{O}}$ are constant on each side of the reaction and change at $P = P_R$.

We are here interested in fundamental features of (de)hydration coupled with fluid flow and solid deformation and, therefore, approximate the relation between densities and P_f, resulting from thermodynamic calculations with Perple_X, with a simple analytical equation. Two effects control the variation of ρ_s and ρ_f with a variation of P_f: First, the elastic compressibility, quantified by β_s and β_f, respectively, and second, the amount of change in solid density across the reaction, quantified by $\Delta\rho_s^R$. Consequently, we approximate the dependence of ρ_s and ρ_f on P_f by

$$\rho_s = \rho_{s0}\big(1 + \beta_s(P_f - P_R)\big) + \Delta\rho_s^R \frac{P_f - P_R}{\Delta P_f + P_f - P_R},$$
$$\rho_f = \rho_{f0}\big(1 + \beta_f(P_f - P_R)\big) \tag{28}$$

where ΔP_f is the width of the P_f interval within which the change in ρ_s occurs. ϕ depends on the density of the solid without the mobile, structurally bound water. We refer to this density as the immobile solid density, $\rho_{im} = \rho_s\big(1 - C_s^{\text{H}_2\text{O}}\big)$. We also approximate the relation between ρ_{im} and P_f with

$$\rho_{im} = \beta_{im}(P_f - P_R) + \Delta\rho_{im}^R \frac{P_f - P_R}{\Delta P_f + P_f - P_R}, \tag{29}$$

where $\Delta\rho_{im}^R$ is the magnitude of the change in ρ_{im} across the reaction. In the numerical algorithm, we will use the approximation for ρ_{im} to calculate ϕ.

4. Results

4.1. Overview

We first present the thermodynamic results and their representative approximations. Then, we present the results from the hydro-mechanical, HM, models (model I and II). Subsequently, we show the results from the hydro-chemical, HC, model (model III), and then from the HMC model (model IV). We focus on the dehydration and hydration scenarios mentioned in our hypothesis since the main results for the dehydration-inflow scenario closely resemble the results of the hydration scenario. An overview of the main features of the presented models is given in Table 2. For model III and IV we also present systematic results for reaction-induced porosity generation during (de)hydration. Finally, we present the results of a systematic analysis with HC model III to determine the parameters controlling the width of (de)hydration zones.

4.2. Thermodynamic Results and Their Approximations

For the dehydration of antigorite serpentinite (i.e., the SOR), Equation 26, at 500°C the values of ρ_s have been calculated with Perple_X. The value of ρ_s exhibits a sharp decrease from ca. 3,200 to ca. 2,550 kg/m³ when the minerals transform from forsterite into antigorite + brucite (Figure 4a). The higher-density solid forsterite is on the low-pressure side of the reaction and the lower-density solid antigorite + brucite is on the high-pressure side of the reaction (Figure 4a). The reaction occurs at $P_R = 1.265$ GPa. For P smaller and larger than P_R the values of ρ_s slightly increase with increasing P due to elastic compressibility (Figure 4a), which is quantified by the compressibility parameter β_s. Values of ρ_f (not displayed) increase monotonously from ca. 1,025 to ca. 1,125 kg/m³ for P from 1 to 1.55 GPa due to compressibility β_f. The value of $1 - C_s^{H_2O}$ for forsterite is 1 and for antigorite + brucite is 0.83 (Figure 4b). With ρ_s, ρ_f and $1 - C_s^{H_2O}$ as function of P we can calculate the variation of ϕ with P using Equation 14. We assume that $\phi = 0$ in the serpentinite, which represents the initial rock (Figure 4c). The dehydration of serpentinite forms forsterite with a porosity of ca. 0.33, required to store liberated water (Figure 4c). With ρ_s, ρ_f, and ϕ we can calculate the total density, ρ_T, as function of P (Figure 4a). In contrast to ρ_s, values of ρ_T increase with increasing P across the reaction. In fact, ρ_T of any system must increase with increasing P so that the compressibility is positive, and the system is thermodynamically stable (e.g., Callen, 1998; Landau & Lifshitz, 1980).

For the GER, which represents the hydration of granulite facies rock, Equation 27, we perform also Perple_X calculations (Bras et al., 2023) to obtain relations between ρ_s, ρ_T, $1 - C_s^{H_2O}$ and ϕ with increasing P (Figures 4d–4f). The value of ρ_s exhibits a sharp increase from ca. 2,700 to ca. 3,228 kg/m³ when the reaction from granulite to eclogite facies occurs (Figure 4d). The reaction occurs at $P_R = 1.941$ GPa. Values of ρ_f (not displayed) increase monotonously from ca. 987 to ca. 1,250 kg/m³ for P from 1.2 to 3.2 GPa due to compressibility β_f. The value of $1 - C_s^{H_2O}$ for granulite is 1 and for eclogite is 0.993 (Figure 4e). We assume that $\phi = 0$ in the granulite, which represents the initial rock (Figure 4f). The hydration of granulite requires a porosity of ca. 0.16 in the eclogite so that water for the hydration can be provided (Figure 4f). Values of ρ_T increase again with increasing P across the reaction, as required by thermodynamic stability (Figure 4d).

For the following numerical simulations, we approximate the relations between ρ_s, ρ_f, ρ_{im}, $1 - C_s^{H_2O}$, ϕ and P using Equations 28 and 29 (Figure 5). These approximations also yield an approximation for the change of ρ_T with changing P (Figures 5a and 5d). Applying these approximations has two reasons: First, we want to make the simulations as general as possible and the approximations include parameters, which can be determined for any metamorphic reaction, namely the three compressibilities $\beta_{s,f,im}$, and the two parameters $\Delta\rho_s^R$ and $\Delta\rho_{im}^R$ which quantify how much ρ_s and ρ_{im}, respectively, change across the reaction. The parameter ΔP_f specifies the width of the P-interval over which the reaction takes place. Such P-interval can, for example, represent the transition zone for divariant reactions. In systematic simulations presented later, we vary the value of ΔP_f to consider simulations with a sharper, mimicking an univariant reaction, and smoother, mimicking a divariant reaction (e.g., Padrón-Navarta et al., 2013; Philpotts & Ague, 2022; Plümper et al., 2017), variation of densities across the reaction (Appendix D and Figure A1). Second, using explicit functions in the numerical algorithm to describe the relations between ρ_s, ρ_f, ρ_{im}, $1 - C_s^{H_2O}$, ϕ and P avoids the need to interpolate between the numerical values and the
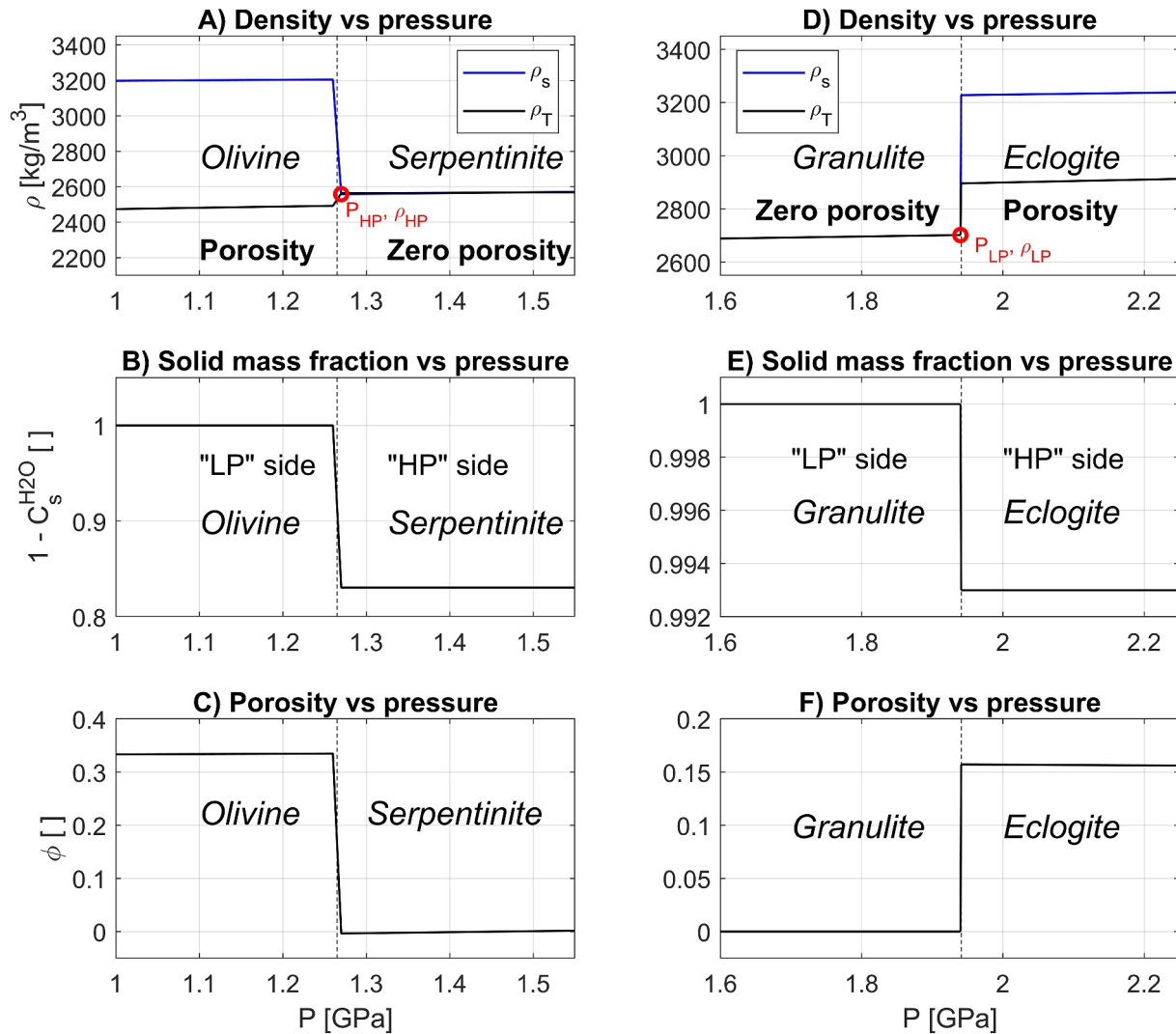
Figure 4. Profiles of densities, mass fraction and porosity versus thermodynamic pressure for the considered dehydration (a–c) and hydration (d–f) reaction. The density versus pressure relations have been calculated using the Perplex_X software (Connolly, 2005). See text for the details on the reactions.

thermodynamic results calculated externally with Perple_X. For the numerical simulations, we will need the relations between ρ_s, ρ_f, ρ_{im}, ϕ, and P only on one side of the reaction, since on one side $\phi = 0$ and consequently $\rho_s = \rho_T$ (Figure 4). For the SOR, we refer to the density value for which $\rho_s = \rho_T$ just across the reaction as ρ_{HP} because this value occurs on the high-pressure side of the reaction (Figures 4a and 5a). The corresponding value of P we term P_{HP} (Figures 4a and 5a). Similarly, for the GER, we refer to the density value for which $\rho_s = \rho_T$ just across the reaction as ρ_{LP} because this value occurs on the low-pressure side of the reaction (Figures 4d and 5d and solid line). The corresponding value of P we term P_{LP} (Figures 4d and 5d solid line).

The applied parameterization for the brucite-out SOR (Figures 5a–5c) is also applicable to the antigorite-out reaction for a positive Clapeyron slope, mentioned above, because the corresponding changes in ρ_s, ρ_f, ρ_{im}, and $1 - C_s^{H_2O}$ are similar for the two reactions when crossing the reaction boundary from low to high values of P (e.g., Malvoisin et al., 2015).

Furthermore, the parameterizations for ρ_s and ϕ for the GER (solid line in Figure 5d) applies also to the antigorite-out reaction with a negative Clapeyron slope. For a negative slope, the antigorite with lower ρ_s is on the low-pressure side of the reaction and the enstatite + forsterite with higher ρ_s are on the high-pressure side. Hence, the GER and the antigorite-out reaction with a negative Clapeyron slope exhibit a similar increase in ρ_s when crossing the reaction boundary from low to high pressure (solid and dashed lines in Figure 5d). The main
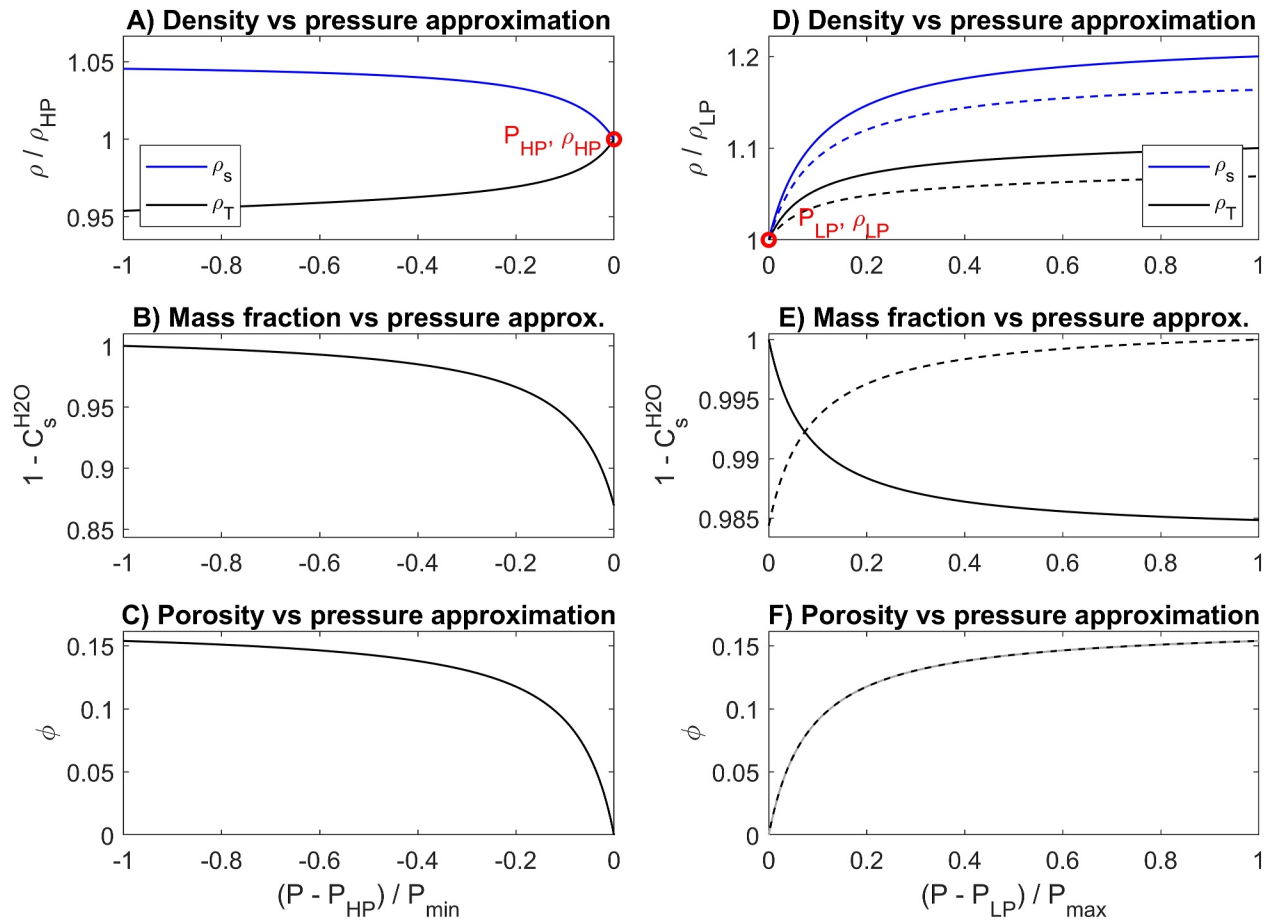
Figure 5. Parameterized relationships of densities (a and d), mass fraction (b and e) and porosity (c and f) vs. thermodynamic pressure applied in the numerical simulations. Only the relationships on the side of the reaction where solid density, ρ_s, and total density, ρ_T, are different are parameterized. For orientation, the circles with coordinates P_{HP}, ρ_{HP} in panel (a) and P_{LP}, ρ_{LP} in (d) indicate the same points as indicated in the density versus pressure relation resulting from Perple_X (see Figures 4a and 4d). The dashed lines in panels (d–f) show the parameterizations applied for a simulation corresponding to the dehydration-inflow scenario for which results are presented in Figures 9g–9i. Symbols are explained in Table 1.

difference between the GER and the antigorite-out reaction with a negative Clapeyron slope is that for the GER the rock with structurally bound H_2O is on the high-pressure side of the reaction while it is on the low-pressure side for the antigorite-out reaction with a negative Clapeyron slope. This difference can be parameterized with a different profile of $1 - C_s^{H_2O}$ versus P. The dashed line in Figure 5e shows a profile of $1 - C_s^{H_2O}$ versus P which corresponds to reactions similar to the antigorite-out reaction with a negative Clapeyron slope: toward higher P there is no more structurally bound H_2O which corresponds to enstatite + forsterite. The applied parameterizations for ρ_s and $1 - C_s^{H_2O}$ provide the same variation of ϕ versus P (superposed solid and dashed lines in Figure 5f). We will show further below that the parameterizations for the antigorite-out reaction with a negative Clapeyron slope (dashed lines in Figures 5d–5f) generate the dehydration-inflow scenario mentioned in the hypothesis.

To emphasize the general applicability of these relations we present them with dimensionless quantities. For the dehydration scenario, represented here by the SOR, values of densities are divided by ρ_{HP} and for the hydration scenario, represented here by the GER, values of densities are divided by ρ_{LP}. For P, for dehydration, we subtract P_{HP} from P and divide the difference by the minimum pressure, P_{min}, of the considered density profile. The dimensionless P is then $(P - P_{HP})/P_{min}$ and varies from -1 to 0 (Figures 5a–5c). For P, for hydration, we subtract P_{LP} from P and divide the difference by the maximum pressure, P_{max}, of the considered density profile. The dimensionless P is then $(P - P_{LP})/P_{max}$ and varies from 0 to 1 (Figures 5d–5f).
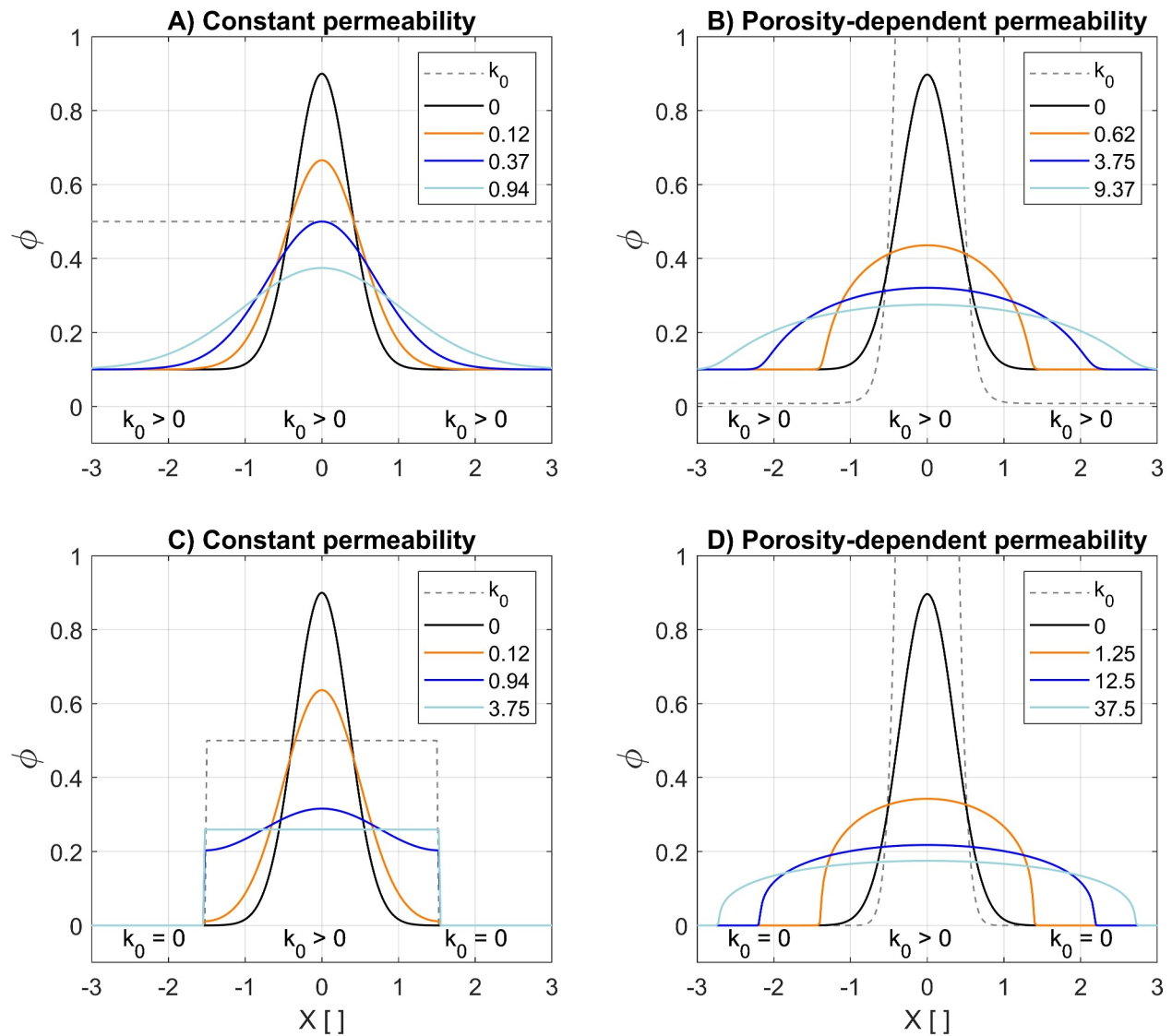
Figure 6. Numerical results of the HM models I (panels a and c) and II (b and d) showing the evolution of porosity, ϕ, with dimensionless time (displayed in legend). For models in panels (a) and (b) the initial permeability, k_0, in the lateral model domains is larger than zero while for models in panels (c) and (d) the initial permeability is zero. See also Table 2 for the characteristics of the models.

4.3. Diffusion-Type HM Models Without Reaction (Models I and II)

We present numerical results for the linear and nonlinear Equations 6 and 9, respectively. For the linear case, the permeability can be either constant in space and time or is initially variable in space but does not change in time. For the nonlinear case, the permeability is a function of ϕ and can vary in space and time. We illustrate the impact of a ϕ-dependent permeability and show that fluid infiltration into an initially zero-porosity, zero-permeability region is feasible for a ϕ-dependent permeability (Figure 6). The diffusion equations are formulated for ϕ which represents the unknown variable and is calculated numerically. For the variable permeability, $k = k_{ref}(\phi/\phi_{ref})^n$, we assume that $k_{ref} > 0$ always so that $k = 0$ only if $\phi = 0$. The profiles of the initial porosity, ϕ_0, are described by a Gaussian distribution and the initial permeability distribution is termed k_0 (Figure 6). For models with variable permeability, the applied value for ϕ_{ref} is the average value of the maximum and minimum value of ϕ_0.

For scenarios with $k_0 > 0$ everywhere in the model domain, ϕ diffuses across the entire model domain for both constant (Figure 6a) and ϕ-dependent (Figure 6b) permeability. The evolving ϕ-profiles for constant and ϕ-
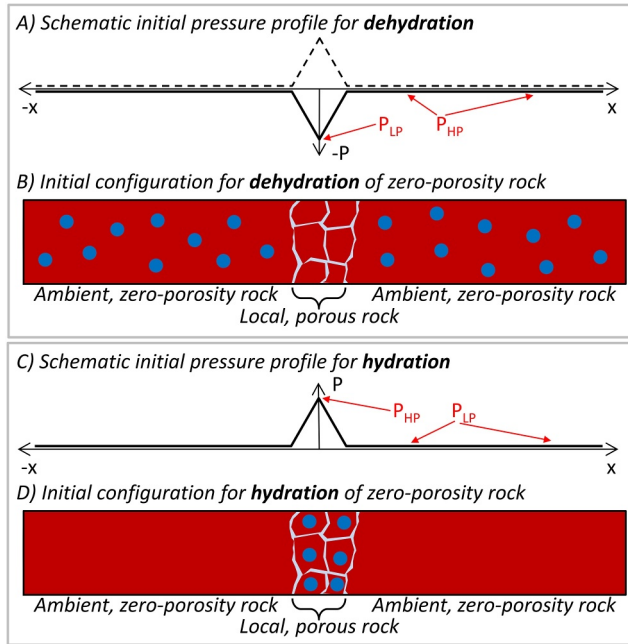
Figure 7. Sketch of the model configuration for a dehydration scenario (panels a and b) and a hydration scenario (c and d). Panels (a) and (c) show the applied initial fluid pressure distribution and (b) and (d) show the initial distribution of porosity and rock with and without structurally bound water (see Figure 3). The dashed line in (a) shows the initial fluid pressure distribution applied for a simulation corresponding to the dehydration-inflow scenario for which results are presented in Figures 9g–9i.

dependent permeability have a different geometry and the ϕ-profiles for ϕ-dependent permeability have a steeper diffusion front (Figures 6a and 6b). For scenarios with $k_0 > 0$ only in the center of the model domain and $k_0 = 0$ in the lateral regions, ϕ diffuses into the zero-permeability domain only for ϕ-dependent permeability (Figures 6c and 6d). For constant permeability, values of $\phi > 0$ cannot propagate into regions where $k_0 = 0$ because k cannot change with time. Values of ϕ become constant in the region where $k_0 > 0$ and the diffusion stops (Figure 6c). In contrast, for ϕ-dependent permeability values of $\phi > 0$ can propagate into regions where $k_0 = 0$, because the permeability is a function of ϕ (Figure 6d). For ϕ-dependent permeability, the diffusion front exhibits sharp, nearly vertical profiles of ϕ. The diffusion of a quantity into a region with initially zero diffusivity is a well-known phenomenon of so-called nonlinear degenerate second-order parabolic equations (e.g., Barenblatt et al., 2000; Kalashnikov, 1987).

4.4. Representative HC Numerical Simulations of (De)hydration and Porosity Generation (Model III)

Based on the thermodynamic results, we consider two 1D model configurations for the simulations involving reactions (Figure 7). For the configuration for simulations with dehydration (Figures 7a and 7b), we assume a narrow central region consisting of rock without structurally bound H_2O which is bounded by two large regions consisting of rock with structurally bound H_2O and zero-porosity. This configuration applies to the SOR. Based on the thermodynamic results, P in the central region must be smaller than in the lateral regions to potentially trigger the SOR (Figure 7a). The initial value of P in the lateral regions represents the ambient pressure that is constant during the simulation and P in the central region represents an initial negative perturbation from the ambient pressure. For the hydration configuration (Figures 7c and 7d), we assume a narrow central region consisting of rock with structurally bound H_2O and with porosity which is bounded by two large regions consisting of rock without structurally bound H_2O and zero porosity. This configuration applies to the GER. Based on the thermodynamic results, P in the central region must be larger than in the lateral regions to potentially trigger the GER (Figure 7c). The initial value of P in the lateral regions represents the ambient pressure that is constant during the simulation and P in the central region represents an initial positive perturbation from the ambient pressure.

For comparison reasons, we apply the relations between ρ_s, ρ_f, ϕ, and P presented in Figure 5 for both the (de)hydration simulations, because the absolute magnitudes of variations of ρ_s, ρ_f, and ϕ with varying P are similar for these relations. We also perform a simulation for the parameterization indicated by the dashed lines in Figures 5d to 5f which corresponds to the dehydration-inflow scenario we mentioned in the hypothesis. For the dehydration-inflow scenario the model configuration is the same as for the dehydration scenario except that there is a positive pressure perturbation in the central domain (dashed black line in Figure 7a). A main difference between the simulations is the absolute magnitude of variation of $1 - C_s^{H_2O}$, which is significantly larger for the dehydration scenario (Figures 4b and 5b) than for the hydration and dehydration-inflow scenario (Figures 4e and 5e).
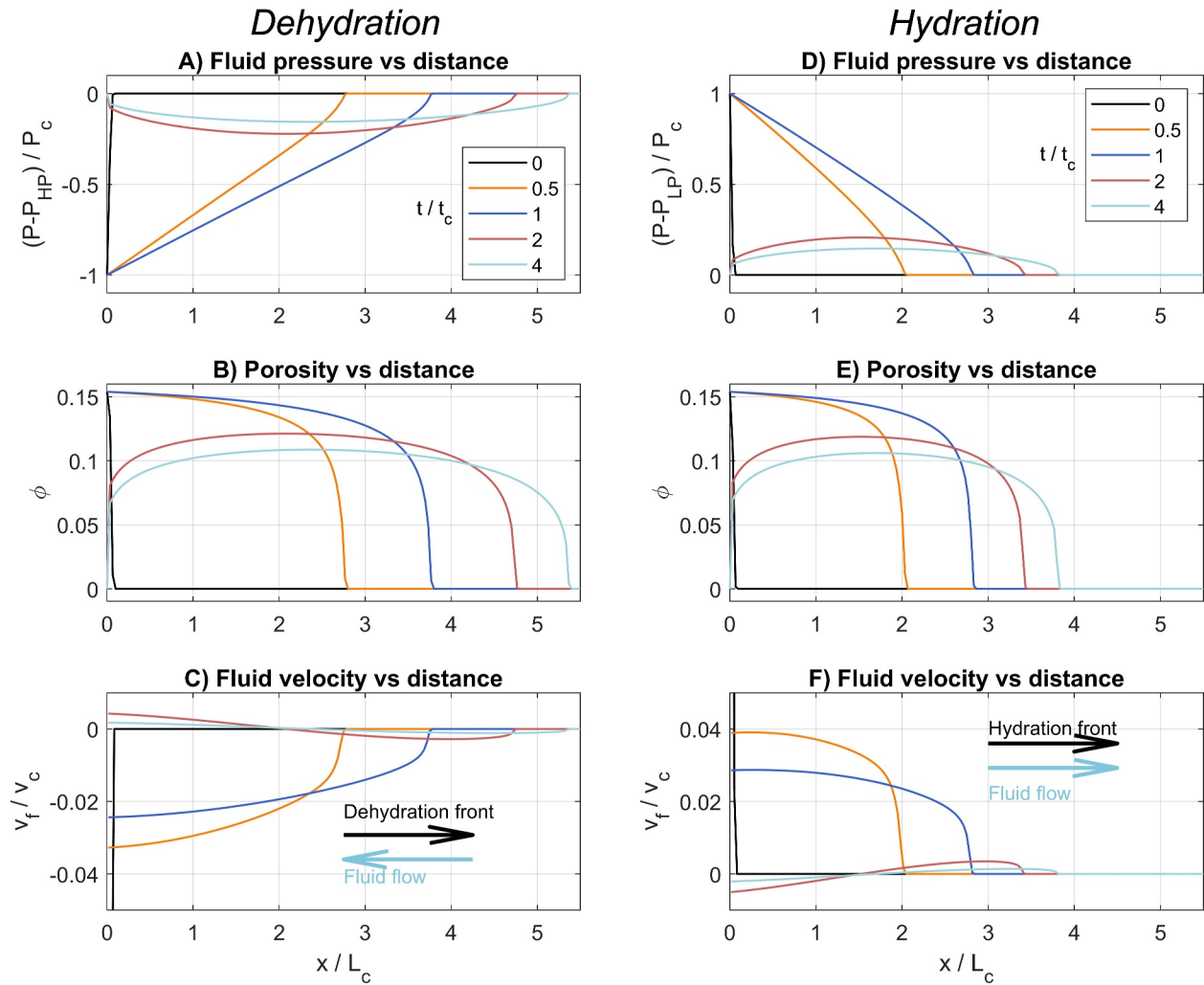
We refer now to the pressure as P_f because changes in pressure occur only in regions with $\phi > 0$. We present all numerical results in dimensionless form. We use three characteristic scales for the nondimensionalization: the characteristic time, t_c, is the duration of the applied pressure perturbation which drives the (de)hydration; the characteristic pressure, P_c, is the absolute magnitude of the applied pressure perturbation, which in our model is the absolute difference between the pressure applied at the left and right model side; and the characteristic hydraulic parameter, $k_c = k_{ref}/\eta_f$. With these three scales we calculate the characteristic length, $L_c = \sqrt{t_c P_c k_c}$, and the characteristic velocity, $v_c = L_c/t_c$. For dehydration simulations, we display the dimensionless pressure $\tilde{P}_f = (P_f - P_{HP})/P_c$ and for the hydration simulation $\tilde{P}_f = (P_f - P_{LP})/P_c$ (see also Figure 5). For both hydration and dehydration simulations, we remove the pressure perturbation after the time t_c so that for model times $> t_c$ the values of $\tilde{P}_f = 0$ at both model boundaries. Setting $\tilde{P}_f = 0$ represents a stop in the fluid supply and we

Figure 8. Representative numerical simulations with the HC model III for dehydration (panels a–c) and hydration scenarios (d–f; see also Table 2 for model characteristics). Panels (a) and (d) show spatial profiles of the temporal evolution of the dimensionless fluid pressure (also referred to as $\tilde{P}_f$ in the text), (b) and (e) the evolution of porosity and (c) and (f) the evolution of the dimensionless fluid velocity (also referred to as $\tilde{v}_f$; see text for nondimensionalization). The different profiles correspond to different dimensionless times. The legend in panel (a) applies to panels (a) to (c) and the legend in (d) to panels (d) to (f). The arrows in panels (c) and (f) indicate the propagation direction of the (de)hydration front and the direction of fluid flow.

continue the simulations until the fluid pressure gradients inside the model domain are significantly decreased by hydraulic diffusion so that the propagation of the (de)hydration front becomes negligibly slow. For both hydration and dehydration simulations, the value of ϕ_{ref} is the maximum value of the initial porosity profile. Therefore, the maximum value of k in the simulations is given by k_{ref}.

For the simulation for the dehydration configuration (Figures 7a and 7b), $\tilde{P}_f$ is initially constant inside the model except at the left boundary, where it is smaller (Figure 8a). With progressive time, the region with $\tilde{P}_f < 0$ becomes wider and within this region the profile of $\tilde{P}_f$ is approximately a straight line (Figure 8a). For the applied parameters, the maximal ϕ is ≈0.15. The region with $\phi > 0$ widens and values of ϕ are close to 0.15 in most of this region (Figure 8b). The front of the dehydration zone propagates in the direction of positive x-coordinates, toward the right model side. While $\tilde{P}_f = -1$ at the left model boundary, values of the dimensionless fluid velocity, $\tilde{v}_f = v_f/v_c$, are always negative which means that the fluid flows in direction of the negative x-coordinate, that is in the opposite direction compared to the propagation direction of the dehydration front (Figure 8c). Once $\tilde{P}_f = 0$ at the left model boundary, the propagation of the dehydration front slows down significantly and the fluid pressure variation across the model continuously decreases due to hydraulic diffusion.

For the hydration configuration (Figures 7c and 7d), $\tilde{P}_f$ is initially also constant inside the model except at the left boundary, where it is larger (Figure 8d). With time, the region with $\tilde{P}_f > 0$ becomes wider and within this region the profile of $\tilde{P}_f$ is approximately a straight line (Figure 8d). Since we applied the same parameters as for the dehydration simulation, the maximal ϕ is also ≈ 0.15 (Figure 8e). The front of the hydration zone propagates in the direction of positive x-coordinates, toward the right model side. Values of $\tilde{v}_f$ are always positive which means that the fluid flows in the direction of the positive x-coordinate, that is in the same direction as the propagation direction of the hydration front (Figure 8f). Like for the dehydration simulation, once $\tilde{P}_f = 0$ at the left boundary, the propagation of the hydration front slows down and the fluid pressure variation across the model continuously decreases.
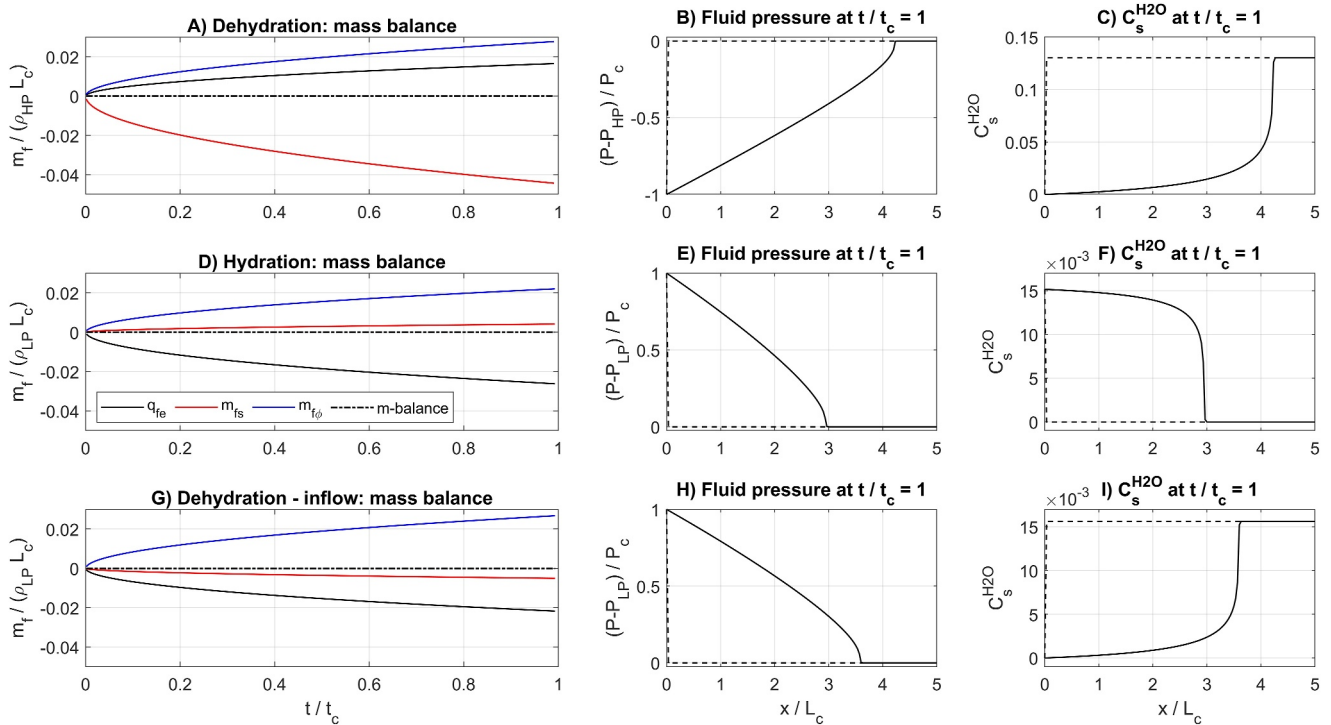
The simulation results for the dehydration-inflow scenario are essentially the same as for the hydration scenario. The main difference between the hydration and dehydration-inflow simulations is that for the dehydration-inflow simulation, the porosity is generated by dehydration and consequently a dehydration front is propagating.

To study the fluid mass balance during the simulations, we calculate the time evolution of the fluid mass in the model domain until $t/t_c = 1$. There are three different fluid masses in our model domain that must be balanced: The fluid mass that is liberated or taken up during (de)hydration, termed m_{fs}, the fluid mass that is stored in the porosity, termed $m_{f\phi}$, and the externally derived fluid mass that flows in or out of the model domain, termed q_{fe}. To calculate the time evolution of these three fluid masses in the model domain, we integrate at every numerical time step each fluid mass in the x-direction over the model domain and then integrate these fluid masses over time. The three fluid masses evolve with time and can be calculated by

$$
m_{f\phi}(t) = \int_0^t \int_0^{Lx} \left(\frac{\partial\left(\phi\rho_f\right)}{\partial t} \right) dx dt' = \left(\int_0^{Lx} \phi\rho_f dx \right) \Bigg|_{t'=0}^{t'=t}
$$

$$
m_{fs}(t) = \int_0^t \int_0^{Lx} \left(\frac{\partial\left((1-\phi)\, C_s^{\mathrm{H_2O}}\rho_s\right)}{\partial t} \right) dx dt' = \left(\int_0^{Lx} (1-\phi)C_s^{\mathrm{H_2O}}\rho_s dx \right) \Bigg|_{t'=0}^{t'=t}, \tag{30}
$$

$$
q_{fe}(t) = \int_0^t \int_0^{Lx} \left(\frac{\partial\left(v_f\phi\rho_f\right)}{\partial x} \right) dx dt' = -\int_0^t \left(v_f\phi\rho_f \right) \Big|_{x=0} dt'
$$

where Lx is the width of the model domain. We calculate the integrals numerically. During the simulations, the total fluid mass must be balanced which means that the sum of the three fluid masses must remain zero during the simulations (Figures 9a, 9d, and 9g). In the simulations for the dehydration, hydration and dehydration-inflow scenario the total fluid mass is always balanced showing both the correctness of the mass balance calculations and the conservativeness of the applied numerical scheme (Figures 9a, 9d, and 9g). For the dehydration scenario, some of the liberated mass of H_2O (red line in Figure 9a) is stored in the porosity (blue line in Figure 9a) and the remaining liberated H_2O that cannot be stored in the porosity flows out of the model domain (black line in Figure 9a, a positive value of q_{fe} indicates outflow). For the hydration scenario, most of the mass of H_2O that flows into the model domain (black line in Figure 9d, a negative value of q_{fe} indicates inflow) is stored in the porosity (blue line in Figure 9d) and a small amount of mass of H_2O is taken up by the solid (red line in Figure 9d). For the dehydration-inflow scenario, all of the mass of H_2O that flows into the model domain (black line in Figure 9g, a negative value of q_{fe} indicates inflow) is stored in the porosity (blue line in Figure 9g) and additionally a small amount of mass of H_2O is liberated by the solid (red line in Figure 9d) and is also stored in the porosity. For comparison, the fluid pressure distribution for the dehydration scenario shows an underpressure at the left model side indicating H_2O outflow (Figure 9b) whereas for the hydration and dehydration-inflow scenarios the fluid overpressure at the left side indicates inflow (Figures 9e and 9h). The distribution of $C_s^{\mathrm{H_2O}}$ indicates the result of the dehydration front propagation for the dehydration and dehydration-inflow scenarios (Figures 9c and 9i) and of the hydration front propagation for the hydration scenario (Figure 9f).

For any (de)hydration reaction corresponding to the considered scenarios, the porosity can be calculated with Equation 14, which assumes that the initial rock has $\phi_0 = 0$. For dehydration, the initial rock with $\phi_0 = 0$ is on the high-pressure (HP) side of the reaction whereas for hydration the initial rock with $\phi_0 = 0$ is on the low-pressure

Figure 9. Fluid mass balance during (de)hydration simulations based on the HC model III. Panels (a–c) show results for the dehydration simulation presented in Figures 8a–8c. Panel (a) shows the fluid mass balance with time until $t/t_c = 1$. The legend is displayed in panel (d). The label q_{fe} indicates the flow of external fluid, with positive values indicating flow out of the model domain, m_{fs} indicates the fluid mass liberated by dehydration (negative) or taken up by hydration (positive), $m_{f\phi}$ indicates the fluid mass stored in the porosity and m-balance represents the mass balance, that is, $q_{fe} + m_{fs} + m_{f\phi}$. Panel (b) shows the spatial distribution of the dimensionless fluid pressure (also referred to as $\tilde{P}_f$ in the text) at $t/t_c = 1$ (dashed line indicates initial distribution). Panel (c) shows the spatial distribution of fluid mass structurally bound in the solid at $t/t_c = 1$ (dashed line indicates initial distribution). Panels (d–f) show the corresponding results for the hydration simulation presented in Figures 8d–8f. Panels (g–i) show results for a simulation like the hydration simulation shown in panels (d–f) but for a dehydration reaction; compare red lines in panels (d) and (g). This simulation corresponds to the dehydration-inflow scenario mentioned in the hypothesis (Section 2).

(LP) side of the reaction (Figures 7 and 8). To display general results for ϕ for both (de)hydration on the same diagram, we apply the relation between ϕ and the ratio $\rho_{s0}(1 - C_{s0}^{H_2O})/\rho_s(1 - C_s^{H_2O})$ given in Equation 14. The ratio represents the mass ratio of the immobile solid mass before the reaction to the immobile solid mass after the reaction. However, we do not plot ϕ versus the parameter $\rho_{s0}(1 - C_{s0}^{H_2O})/\rho_s(1 - C_s^{H_2O})$, because general results for hydration and dehydration would look identical. Instead, we plot ϕ versus the ratio $\rho_{sHP}(1 - C_{sHP}^{H_2O})/\rho_{sLP}(1 - C_{sLP}^{H_2O})$ where quantities with subscript "HP" refer to the quantities on the high-pressure side of the reaction and with subscript "LP" to quantities on the low-pressure side. For the considered dehydration reaction, $\rho_{sHP} < \rho_{sLP}$ and $1 - C_{sHP}^{H_2O} < 1 - C_{sLP}^{H_2O}$ whereas for hydration, $\rho_{sHP} > \rho_{sLP}$ and $1 - C_{sHP}^{H_2O} < 1 - C_{sLP}^{H_2O}$ (Figure 4). If the ratio $\rho_{sHP}(1 - C_{sHP}^{H_2O})/\rho_{sLP}(1 - C_{sLP}^{H_2O}) = 1$, then no porosity is generated during (de)hydration. If this ratio <1 for a reaction, then porosity is generated during dehydration while if this ratio >1 then porosity is generated during hydration (Figure 10a). Equation 14 shows that porosity generation during (de)hydration does not only depend on the change of ρ_s but also on the change of $C_s^{H_2O}$. Figure 10b displays the contours of ϕ for corresponding values of the mass fraction ratio on the horizontal axis and solid density ratios on the vertical axis. As examples, we indicate the corresponding ratios of solid density and mass fraction for several (de)hydration reactions (see caption of Figure 10b).

4.5. Representative HMC Numerical Simulations of (De)hydration and Porosity Generation (Model IV)

We perform two similar (de)hydration simulations as in the section above, but we now consider additionally the solid volumetric deformation by poroviscous compaction and decompaction. This (de)compaction and associated spatial variations in solid and fluid velocities occur over a characteristic length scale that is termed the compaction
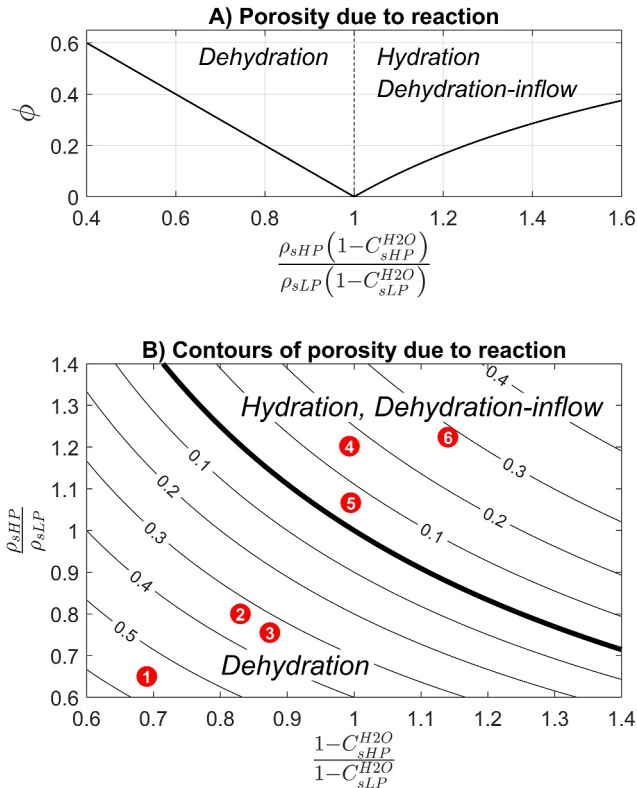
Figure 10. Porosity, ϕ, as function of solid density and mass fraction ratios. Porosity is calculated with Equation 14. Symbols are explained in Table 1. (a) Profile of porosity versus combined solid density and mass fraction ratio. Subscript "HP" indicates that the corresponding quantity is on the high-pressure side of the reaction and subscript "LP" that it is on the low-pressure side (see also Figure 5). (b) Contours of porosity versus mass fraction ratio and solid density ratio. The red circles with numbers indicate the ratios for particular mineral reactions that are described in the corresponding references: (1) Dehydration of brucite to periclase (Schmalholz et al., 2020); (2) Dehydration of antigorite + brucite to forsterite (Schmalholz et al., 2023); (3) Dehydration of serpentinite to dunite (Malvoisin et al., 2015, 2021); (4) Hydration of granulite to eclogite (Bras et al., 2023); (5) Hydration of granulite to eclogite (Centrella, 2019); (6) Dehydration-inflow scenario for antigorite breakdown to forsterite + enstatite for a negative Clapeyron slope, that is, antigorite is on the low-pressure side of the reaction (densities after Malvoisin et al., 2015; their Figure 1A).

length (e.g., McKenzie, 1984). The compaction length is proportional to the value of $\sqrt{\eta_\phi k / \eta_f}$ (e.g., McKenzie, 1984). We assume that the characteristic scale in our model, L_c, is like the compaction length of our model and, hence, apply as compaction viscosity the value of L_c^2 / k_c. The overall evolution of $\tilde{P}_f$ and ϕ is similar for the corresponding simulations with and without solid deformation (Figures 8 and 11). However, for simulations with solid volumetric deformation, ϕ varies now in space and time on the left model side (Figure 11). For dehydration, ϕ is decreasing and the largest decrease occurs at the left model boundary (Figure 11b) where the rock volume is decreasing the most ($V/V_0 < 0$; Figure 11c). Values of $\tilde{P}_f$ are negative and smallest on the left model side indicating values of P_f which are smaller than the total rock pressure, P. This fluid underpressure causes a decrease in V (Equations 19 and 22; Figure 11c). For the hydration simulation the situation is opposite, and a fluid overpressure causes ϕ and V to increase on the left model side (Figures 11d–11f). Figures 8 and 11 show that the velocity of the dehydration front is not considerably affected by the solid deformation because the front shifts a similar distance within the same time.
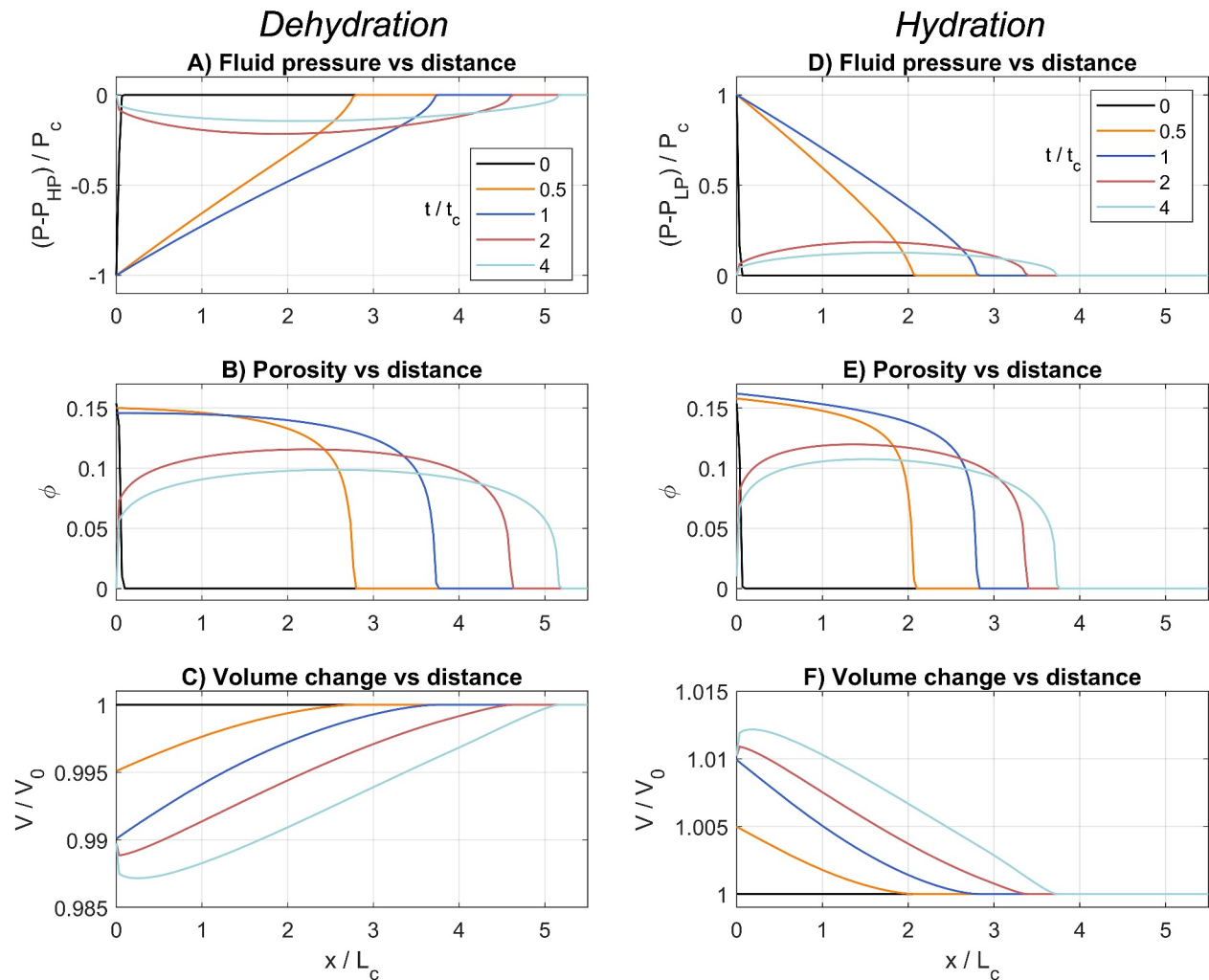
Like in Figure 10, we plot the variation of ϕ for a variation of the ratio of $\rho_{sHP}(1 - C_{sHP}^{H_2O}) / \rho_{sLP}(1 - C_{sLP}^{H_2O})$, and consider additionally a variation of V/V_0 (Figure 12).

For dehydration and no volume change, $V/V_0 = 1$, the ratio $\rho_{sHP}(1 - C_{sHP}^{H_2O}) / \rho_{sLP}(1 - C_{sLP}^{H_2O})$ must be <1 to generate $\phi > 0$ (Figures 10a and 12a). The contours of ϕ indicate that for a fixed value of $\rho_{sHP}(1 - C_{sHP}^{H_2O}) / \rho_{sLP}(1 - C_{sLP}^{H_2O})$, an increase in V/V_0 causes an increase in ϕ.

For hydration and no volume change, the ratio $\rho_{sHP}(1 - C_{sHP}^{H_2O}) / \rho_{sLP}(1 - C_{sLP}^{H_2O})$ must be >1 to generate $\phi > 0$ (Figures 10a and 12b). The contours of ϕ indicate that for a fixed value of $\rho_{sHP}(1 - C_{sHP}^{H_2O}) / \rho_{sLP}(1 - C_{sLP}^{H_2O})$, an increase in V/V_0 also causes an increase in ϕ.

4.6. Systematic Simulations and Application to the Time Scale of (De)hydration

We performed hydration simulations without solid deformation (as displayed in Figures 8d–8f) and vary systematically the value of the porosity exponent, n, and the width, or sharpness ΔP_f, of the density, mass fraction and porosity transition around the hydration reaction (see Figure A1). High values of $n > 5$ can mimic permeability increase due to fractures and different values of ΔP_f cause sharper or smoother density variations across the reaction boundary (Figure A1) which can mimic simpler univariant or more complex bivariant reactions. We run the simulations until the velocity of the hydration front becomes negligibly small after the fluid pressure perturbation was removed at the time t_c. In practice, this situation was achieved when the total simulation time was one order of magnitude longer than t_c. For each simulation, we record the total width L of the hydration zone at the end of the simulation. For n between 1 and 10 and ΔP_f between 0.01 and 0.1 (Figure A1) the simulations show that the dimensionless distance, $L / \sqrt{t_c k_c P_c}$, only varies between 3 and 4.25 (range of contour values in Figure 13). The width of the hydrated region is, hence, only weakly dependent on n and ΔP_f. Therefore, we apply the approximation:

$$L / \sqrt{t_c k_c P_c} \approx 4. \tag{31}$$

We modify Equation 31 in the Section 5.7 to estimate reaction-induced permeabilities in rock.

Figure 11. Representative numerical simulations with the HMC model IV for dehydration (panels a–c) and hydration scenarios (d–f; see also Table 2 for model characteristics). Panels (a) and (d) show spatial profiles of the temporal evolution of the dimensionless fluid pressure (also referred to as $\tilde{P}_f$ in the text), (b) and (e) the evolution of porosity and (c) and (f) the evolution of the solid volume change (see text for nondimensionalization). The different profiles correspond to different dimensionless times. The legend in panel (a) applies to panels (a) to (c) and the legend in (d) to panels (d) to (f).

5. Discussion

### 5.1. Hydro-Mechanical-Chemical Models

There exist many different types of models that describe the coupling of fluid flow, rock deformation, chemical reactions and transfer of heat and mass (e.g., Gerya, 2019; Ghorbani et al., 2016; Katz, 2008; Keller & Suckale, 2019; Pesavento et al., 2017; Roded et al., 2018; Xu et al., 2005). In our model, the (de)hydration reaction and the fluid flow is driven by a fluid pressure perturbation that we apply as a boundary condition. We do not model the process that generates this fluid pressure perturbation. In nature, fluid pressure variations, like fluid underpressure in serpentinite, can be generated by rock deformation, for example, as modeled in Schmalholz et al. (2023). Fluid overpressure could develop during deserpentinization (e.g., Huber et al., 2022; Plümper et al., 2017) especially if gravity-controlled viscous compaction of the rock is considered (e.g., McKenzie, 1984; Scott & Stevenson, 1984). For the considered scenario of hydration of granulite, fluid entered the system likely through fractures and these fluids likely were overpressured, which might have been one of the causes for the fracturing (i.e., hydrofracturing). Also, the hydration front in the granulite propagated in the two directions orthogonal away from the initial fracture (Figure 1a). Hence, fluid flow was not controlled by a gravity-controlled fluid pressure gradient which would cause fluid flow only in the upward direction.
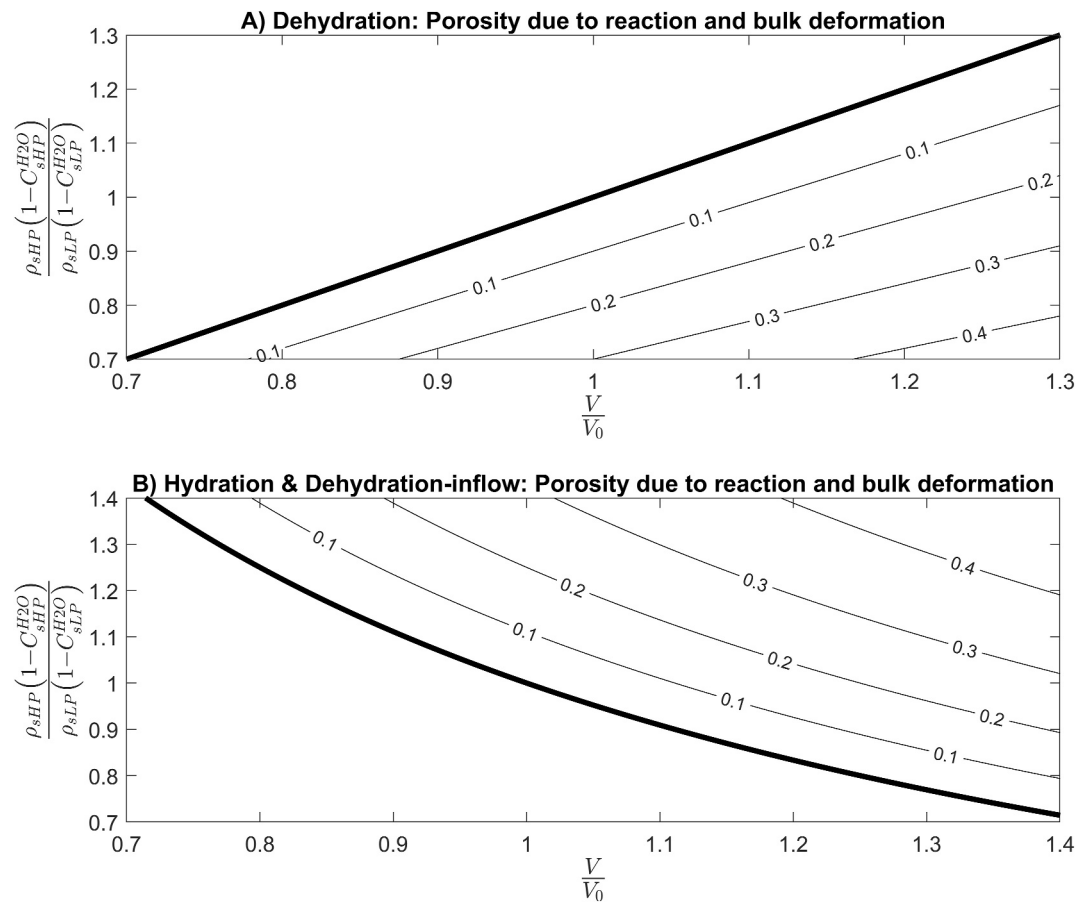
Figure 12. Contours of porosity, ϕ, as function of solid density and mass fraction ratios (vertical axis) as well as solid volume change (horizontal axis). Porosity is calculated with Equation 25. Symbols are explained in Table 1. Subscript "*HP*" indicates that the corresponding quantity is on the high-pressure side of the reaction and subscript "*LP*" that it is on the low-pressure side (see also Figure 5). (a) Contours of porosity for dehydration scenario. (b) Contours of porosity for hydration and dehydration-inflow scenario.

A crucial feature in most existing coupled models is the evolution of the porosity. For example, the importance of porosity variations has been shown by studies on porosity waves that can result from the gravity-driven compaction of poroviscous rock (e.g., McKenzie, 1984; Scott & Stevenson, 1984). Porosity waves are a ubiquitous feature arising from the governing equations of compressible two-phase flow (e.g., McKenzie, 1984; Scott & Stevenson, 1984) and such waves have been observed also in analog experiments (e.g., Scott et al., 1986). Porosity waves are of interest because these waves are a potentially important mechanism of fluid and melt mass transport in the lithosphere (e.g., Bessat et al., 2022; Jordan et al., 2018). Our HMC (de)hydration model IV is relevant for porosity waves because the changes in effective pressure during the propagation of porosity waves could trigger (de)hydration like the applied fluid pressure perturbations in our model. The largest values of effective pressure corresponding to fluid overpressure are likely limited by the tensile strength of rocks, which is in the order of a few tens of MPa (e.g., Perras & Diederichs, 2014).

A key difference between the various coupled two-phase models is the treatment of density changes. In many models, especially in models for melt migration, the densities of the solid and fluid constituents are assumed to be constant (e.g., Aharonov et al., 1995; O. Evans et al., 2018; Jones & Katz, 2018; Katz, 2008; McKenzie, 1984; Schiemenz et al., 2011; Spiegelman, 1993), whereas in other models mainly derived in the context of fluid-rock interaction the densities are determined by thermodynamic calculations, making them variable and consistent with the changing chemical and phase composition of the system (e.g., Beinlich et al., 2020; Huber et al., 2022; Malvoisin et al., 2015; Plümper et al., 2017; Schmalholz et al., 2020, 2023; Vrijmoed & Podladchikov, 2022). The consideration of density changes has an important impact, for example, on the propagation behavior of porosity
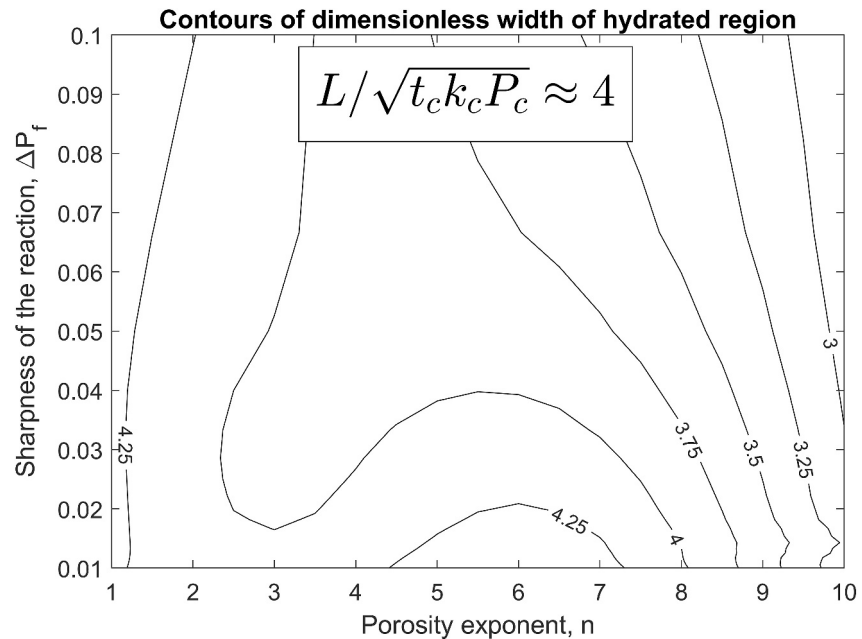
Figure 13. Contours of the dimensionless width, *L*, of the hydration zone resulting from systematic simulations with the HC model III for a hydration scenario. The porosity exponent, *n*, is varied from 1 to 10 and the parameter ΔP_f from 0.01 to 0.1. ΔP_f controls the pressure interval over which the reaction occurs. The applied parameterized density, mass fraction and porosity profiles for $\Delta P_f = 0.01$ and 0.1 are indicated in Figure A1. The geometry of the contours is not important but their values since they only vary between 3 and 4.25 although both *n* and ΔP_f vary each by one order of magnitude.

waves (e.g., Malvoisin et al., 2015; Omlin et al., 2017). Malvoisin et al. (2015) show that density variations related to local equilibrium reactions enable porosity waves to propagate into a medium at the limit of zero initial connected porosity, without any viscous or elastic deformation. Furthermore, Omlin et al. (2017) show that the consideration of the kinetics of the chemical reactions that cause the density variations may enable porosity waves to potentially rise also in low-temperature regimes so that porosity waves are not necessarily limited to the high-temperature, viscous regions in the lithosphere (Chakraborty, 2017).

Several studies have investigated (de)hydration reactions with density changes like the ones studied here (e.g., Beinlich et al., 2020; Huber et al., 2022; Klein & Garrido, 2011; Lacinska et al., 2017; Malvoisin et al., 2015; Picazo et al., 2020; Plümper et al., 2017; Vrijmoed & Podladchikov, 2022). A particular feature of our approach is the addition of viscous volumetric strain of the solid in the analytical expression for the porosity, Equation 25 (Khakimova & Podladchikov, 2024), compared to many previous studies that neglect solid deformation in the porosity calculation (e.g., Beinlich et al., 2020; Huber et al., 2022; Plümper et al., 2017; Vrijmoed & Pod-ladchikov, 2022). Furthermore, we consider both hydration and dehydration scenarios in a unified approach and provide the conditions required for the propagation of hydration or dehydration fronts.

5.2. Importance of Nonlinear Porosity-Permeability Relation for the Sharpness of the Reaction Front

In our model, the mechanism generating the sharpness, or steepness, of the (de)hydration front is governed by the nonlinear relation between porosity and permeability (Figure 6). We have analyzed here the propagation of the reactive (de)hydration front, which is characterized by the propagation of a sharp porosity front, accompanied by evolving porosity and permeability (Figures 8, 11, and 13). We discuss briefly the context between our model and other models of porosity and reaction front propagation.

The propagation of a sharp porosity front can be considered as a particular type of wave motion, like shock waves or jumps in nonlinear kinematic waves (e.g., Bhatnager, 1979; Orr, 2007; Panfilov, 2018; Whitham, 1965). Another mechanism for producing sharp reaction fronts is related to chemical reactions between the fluid and the solid matrix. Recent numerical calculations show that a small difference in the composition of the infiltrating fluid can change the morphology of the reaction zone from a diffusive zone to a considerably sharp front (e.g.,

Guy, 1993; Vrijmoed & Podladchikov, 2022). These numerical results agree with classical findings that indicate the significance of linearity or nonlinearity in the dependence between fluid and solid concentrations (e.g., Fletcher & Hofmann, 1974; Vrijmoed & Podladchikov, 2022). A linear dependence, with constant equilibrium partitioning coefficients between phases, is characteristic of ideal solutions or simple trace element partitioning. Such linear dependence will lead to a linear advection of any inhomogeneities in chemical compositions without changing their shape in space. Conversely, a nonlinear dependence changes the sign of the curvature of the functional dependence of the concentration of a fluid component on the concentration of the same component in the solid. Such nonlinear dependence is characteristic of major chemical components and determines the morphology of the reaction front (e.g., Fletcher & Hofmann, 1974; Vrijmoed & Podladchikov, 2022). The chemical partitioning is nonlinear for all trace and major elements for phase transitions that change the equilibrium phase assemblages (e.g., Vrijmoed & Podladchikov, 2022). In the numerical simulations presented by Vrijmoed and Podladchikov (2022), there is a change in front morphology from a diffusive zone, such as for rarefaction waves in gas dynamics, to a sharp front, such as for shock waves or jumps in nonlinear kinematic waves (e.g., Panfilov, 2018; Whitham, 1965) when the CO_2 concentration in the infiltrating fluid is increased from less than one to over one weight percent. Hence, the propagation of sharp reaction fronts can be caused by a nonlinear porosity-permeability relation, as considered in our model, and/or by a nonlinear dependence between fluid and solid concentrations.

5.3. Importance of Density Variations for Porosity Evolution

A fundamental feature of the thermodynamics of metamorphic and melting reactions is that the density of the solid changes during the reaction. These density variations contribute proportionally to the variations in porosity which significantly affects the permeability resulting from the strongly nonlinear porosity versus permeability relation (e.g., Beinlich et al., 2020; Bessat et al., 2022; Bras et al., 2023; Huber et al., 2022; Malvoisin et al., 2015; Plümper et al., 2017; Schmalholz et al., 2023). Many studies, however, neglect these density changes. Recently, Hu et al. (2022) showed that the assumption of constant density causes a volume error of 15% in their model for melt migration. The reason is that the assumption of constant density degenerates the fundamental equation for the conservation of mass to an equation for the conservation of volume which is not a fundamental law in thermodynamics or continuum mechanics.

In our model, we apply the mass conservation law for the chemically immobile solid component of the system, without the simplifying assumption of constant density. Vrijmoed and Podladchikov (2022) documented this approach for several reactions like the ones considered here. A particular feature of this approach is the calculation of porosity by analytically integrating the mass conservation equation for the immobile solid component. Bessat et al. (2022) extended this approach to a scenario where all components are mobile but, therefore, could not calculate the porosity anymore by analytically integrating a mass conservation equation of an immobile solid component. They had to calculate the porosity numerically. For simplicity, we returned here to a scenario for which the porosity can be calculated by analytical integration of the mass conservation of an immobile solid component. This analytical integration resulted in our Equations 14 and 25.

5.4. Mass Transport

An important question is whether high porosity domains can transport significant pore fluid mass while propagating through low porosity domains because the high porosity domain could propagate similarly to a seismic wave so that pore fluids would only be moved locally but not be transported together with the propagating high porosity domain. Jordan et al. (2018) show that mass can be transported in 2D and 3D porosity waves; a fact that has been doubted based on 1D porosity wave studies. Therefore, porosity waves are a potential mechanism to transport significant fluid and melt mass in a channelized style across the lithosphere-asthenosphere boundary and the viscous lithospheric mantle. In our model, involving regions with zero porosity, the porosity front travels with the same velocity as the chemical alteration front and, hence, must transport the fluid mass.

Porosity waves have been proposed as a mechanism forming observed seismic chimneys above hydrocarbon reservoirs (e.g., Yarushina et al., 2021). The application of decompaction weakening (e.g., Connolly & Podladchikov, 1998, 2007) and the consideration of viscous shear deformation of the solid (Räss et al., 2019) enables a significant channelization of porosity waves for 2D and 3D flow. Furthermore, Connolly and Podladchikov (1998) show that employing a visco-elastic volumetric deformation of the solid enables porosity waves to travel through

rock in the limit of zero initial connected porosity, whereas viscous porosity waves are trapped in the zero-porosity limit and, hence, cannot transport mass into regions with initially zero porosity (e.g., Barcilon & Richter, 1986; Connolly & Podladchikov, 1998, 2015). We show here that porosity fronts are not trapped in the zero-porosity limit in a viscous medium if (de)hydration takes place. Hence, reactive porosity waves are a potentially important mechanism of fluid transport across viscous regions in the limit of zero-connected porosity. Such mass transport by pore fluids in the zero-porosity limit may have been important during the formation of continental crust, as an alternative or complementary mechanism to mass transport by diapirism (e.g., Hacker et al., 2015).

5.5. Discussion of the Hypothesis for (De)hydration Mechanisms

The presented numerical simulations support our hypothesis for reaction-induced porosity generation by (de)hydration front propagation. We considered the two representative reactions SOR and GER (Figure 4). There is a fundamental difference between SOR and GER: For both reactions, the solid with structurally bound H_2O is on the high-pressure side of the reaction, but for the SOR ρ_s decreases across the reaction boundary from lower to higher P (Figure 4a), while for GER, ρ_s increases across the reaction boundary from lower to higher P (Figure 4d). In other words, for the dehydration scenario the reactant (serpentinite) is on the high-pressure side of the reaction and has a smaller ρ_s than the product (olivine). Conversely, for the hydration scenario the reactant (granulite) is on the low-pressure side of the reaction but also has a smaller ρ_s than the product (eclogite). Since the reactant for both hydration and dehydration scenarios always has a smaller ρ_s than the product, the reaction generates porosity and, hence, permeability. Fluid flows always from high to low fluid pressure so that the occurrence of the hydration or dehydration scenarios is controlled by the change of ρ_s across the reaction, namely an increase or decrease of ρ_s with increasing pressure. The thermodynamic results for SOR and GER are representative for a wide range of (de)hydration reactions that can involve zero-porosity rock. The main differences are whether ρ_s increases or decreases when crossing the reaction from lower to higher pressure and whether, consequently, ϕ increases or decreases (Figure 4).

In our model, the rock initially has zero porosity, which means the most unfavorable case for fluids to flow. From a thermodynamic point of view, a zero-porosity rock is consistent with the applied reactions, because they have no free fluid phase on one side of the reaction, implying zero porosity. Concerning the transport model, the zero-porosity case is an end member and representative of rocks with very low permeability and porosity. Ductile serpentinite (as shown in our Figure 1b) at >12 kbar and 500°C likely has such very low porosity and permeability because most of the porosity might have been "closed" by viscous compaction during burial. Estimates for permeability relevant for metamorphism are as low as 10^{-23} m^2 (e.g., Ague, 2014; Katayama et al., 2012) or even lower in serpentinite when extrapolated to confining pressures >10 kbar (e.g., Hatakayama et al., 2017). Also, the granulite in W-Norway (our Figure 1a) was likely extremely dry at its maximum burial depth and, hence, did not transform everywhere into eclogite. A rock such as a "dry" granulite that experiences fluid influx along a fracture network on a large scale (10–1,000s of meters), will be affected by fluid influx from such a fracture-like structure (with a porosity near 1) into the wall rock system (with porosity as low as 10^{-3}; Kaatz et al., 2023) on a small scale (millimeters to meters) as it is valid for the Holsnøy case (our Figure 1a) and would exactly reflect such a case of fluid infiltration into granulite in the limit of zero-permeability. The main fluid pressure gradient-driven flow would occur along the fracture network, but some fluid would be also infiltrating the adjacent low-permeability wall rocks. Therefore, we consider the (de)hydration of zero-permeability rocks as a reasonable endmember for many natural situations in which sharp (de)hydration fronts propagate. Our models also work when the rocks do have an initially small porosity and permeability. If both reactant and product initially have a porosity and a free fluid phase, then more (de)hydration scenarios as considered here may be possible, depending on the initial porosity magnitudes.

For our model, the two representative simulations for the dehydration and hydration scenarios share some common fundamental features, such as the propagation of a sharp reaction front into a rock that is either dehydrated or hydrated. The (de)hydration front is characterized by a strong spatial variation of ϕ to 0 where the profile of ϕ versus x is nearly vertical (Figures 8b, 8e, 11b, and 11e). The timing of (de)hydration is similar and the (de)hydration front propagates with a similar velocity (Figures 8 and 11). The dehydration and hydration scenarios also exhibit some fundamental differences, since for the hydration scenario the hydration front and the fluid move in the same direction while for the dehydration scenario the fluid moves in the opposite direction as the front (Figures 8 and 11).

To quantify and predict (de)hydration front propagation and its consequences on other processes such as fluid migration, faulting and melting, it is not sufficient to study only the chemical aspects of (de)hydration. (De)hydration involves the flow of aqueous fluid, which we refer to here as fluid flow. This fluid flow occurs in porous rock whereby the permeability of these rocks and the fluid viscosity control the length and time scale of fluid flow. Furthermore, porous fluid flow is controlled by gradients in fluid pressure, P_f, which control the velocity and direction of fluid flow. Hence, hydraulic parameters like permeability, fluid viscosity and fluid pressure gradients control the amount of fluid mass that can be transported within a certain time over a certain distance along a certain direction. Furthermore, (de)hydration can also change the rock volume and generate solid deformation which causes stress variations in the rock (e.g., Kelemen & Hirth, 2012; Lindgren, 1912; Plümper et al., 2022; Schmalholz et al., 2020).

For the dehydration-inflow scenario, the change of ρ_s with P is similar to the hydration scenario. A reaction corresponding to this scenario is the breakdown of antigorite to forsterite + enstatite + H_2O for high pressure where the Clapeyron slope of the reaction is negative (e.g., Malvoisin et al., 2015; Ulmer & Trommsdorff, 1995). The antigorite is on the low-pressure side of the reaction and has a smaller ρ_s than forsterite + enstatite (e.g., Malvoisin et al., 2015). Concerning the propagation direction of the reaction front and the direction of fluid flow, the dehydration-inflow scenario is like the hydration scenario.

5.6. Simplifications

To keep the mathematical model as simple as possible but as complex as necessary to capture the fundamental features of (de)hydration font propagation, we applied several simplifications. A main simplification of our model is that we consider only (de)hydration that generates porosity and, hence, permeability. The porosity generation results mainly from the change in solid density associated to (de)hydration. With our simple model, we cannot describe (de)hydration reactions that cause density changes that consume porosity. For example, the opposite reaction of the SOR would be the hydration of olivine to form serpentinite and a more general reaction would be the hydration, or serpentinization, of peridotite. If the peridotite has very low porosity, then the solid density changes associated to the reaction would reduce the porosity to zero because the reaction tends to close porosity (clogging). For such reactions, the porosity cannot be mainly generated by the reaction itself but likely must be generated by significant solid deformation. Important geological examples of such scenario for which porosity is decreased by the reaction are the hydration of high-pressure rocks during exhumation along the plate boundary, such as the transformation of eclogite into blueschist (e.g., van der Straaten et al., 2008), or the serpentinization of the slab mantle during bending-related faulting at the outer rise (e.g., Ranero et al., 2003). Both of these rock transformation processes occur basically in a daily manner and both have major implications for the long-term behavior of the respective subduction zone systems and even the global water budget. Several studies proposed mathematical models to describe and quantify such serpentinization (e.g., O. Evans et al., 2018, 2020; Malvoisin et al., 2021). However, these models still face several challenges. For example, O. Evans et al. (2018, 2020) assume in their model that solid densities are constant during the serpentinization and treated them as constants in their mass conservation equations. Malvoisin et al. (2021) show that there are two different possibilities to treat volume changes in the mathematical model, either by reducing existing pore space (clogging) or by compressing the solid material. More research is required to eventually derive a mathematical model for serpentinization that captures the significant changes in solid density and porosity as well as the solid deformation.

Furthermore, we do not consider the dissolution of solid components into the fluid and the input or loss of solid components into the system. Such dissolution as well as input and loss of solid components is considered important for many pseudomorphic replacement reactions during which the rock volume presumably does not change (e.g., Lindgren, 1912; Putnis, 2009; Putnis & John, 2010), such as the eclogite-to-blueschist conversion (e.g., van der Straaten et al., 2008) mentioned before. Our models can be considered as a starting point for studying replacement reactions with mathematical models.

Moreover, we only consider 1D scenarios and volumetric solid deformation and, hence, neglect shear deformation. Such 2D and 3D shear deformation can have an important impact on channeling of fluid flow (e.g., Räss et al., 2019) or the formation of dehydration veins (e.g., Schmalholz et al., 2023). Furthermore, we consider an isothermal system only and, hence, do not consider heat transfer and the effects of latent heat related to the considered reactions. Such thermal effects can be similarly added to our model as Bessat et al. (2022) have done in their model of reactive porosity waves.

5.7. Estimating Permeabilities of Natural (De)hydration Zones

Measuring values of porosity for metamorphic rocks is challenging. In a sequence of measurements with increasing confinement and temperature the compliant porosity gets closed. Then laboratory-derived data must be extrapolated to the relevant *P-T* conditions (e.g., Katayama et al., 2012; Taetz et al., 2018). Such a procedure is even more complicated for measuring permeability as it must be determined via flow-through experiments, which take very long for very low permeabilities (e.g., Katayama et al., 2012). Importantly, these measured values for porosity and permeability are background values only, as they cannot account for transient reaction-induced changes in the porosity and permeability of the reacting rock (see discussion in Ingebritsen & Manning, 2010). Reaction-induced porosity can be one order of magnitude larger than the background porosity (e.g., John et al., 2012; Taetz et al., 2018). Since permeability scales with a power-law relation with porosity, the related uncertainties for permeability become very large. We show here how the results of our systematic simulations (Figure 13) can be used to estimate bounds for the reaction-induced permeability of natural (de)hydration zones.

Our models III and IV show that the hydration and dehydration of a zone are similar if the corresponding reactions exhibit a similar change in density across the (de)hydration reaction and if the absolute magnitude of the pressure perturbation, driving the (de)hydration, is identical (Figures 8 and 11). Therefore, Equation 31, resulting from systematic hydration simulations, is also applicable to dehydration. To estimate permeabilities from natural (de)hydration zones, we substitute $k_c = k_{ref}/\eta_f$ in Equation 31 and solve for the permeability which yields

$$k_{ref} \approx \frac{L^2 \, \eta_f}{16 \, t_c \, P_c}.$$

(32)

In our simulations, k_{ref} represents the maximum reaction-induced permeability in the (de)hydration zone since we use the maximum porosity in the model as ϕ_{ref} (see Equation 7). In our model, the fluid pressure at the end of (de)hydration, at t_c, varies approximately nearly linearly across the (de)hydration zone with a width of L (Figures 8a and 8d for $t/t_c = 1$). The absolute value of P_c is difficult to estimate for natural situations and for the following applications we introduce the absolute value of the pressure gradient $dP/dL = |P_c/L|$. We further introduce the average propagation velocity of the (de)hydration front as $v_F = L/t_c$. The permeability is then

$$k_{ref} \approx \frac{\eta_f}{16} \frac{v_F}{\frac{dP}{dL}}.$$

(33)

For the following permeability estimations, we assume typical values in the order of $\eta_f = 10^{-4}$ Pas (e.g., Walther & Orville, 1982). However, the permeabilities can easily be recalculated for different viscosity values. For example, if the viscosity is 10^{-3} Pas instead of 10^{-4} Pas the permeability would be a factor of 10 larger according to Equation 33.

Permeabilities in rock can be highly variable (e.g., Ingebritsen & Manning, 2010). Typical values for ductile crustal rocks at depths deeper than ~10 km are between 5×10^{-19} and 10^{-16} m^2 (e.g., Ingebritsen & Manning, 2010). The light gray area in Figure 14 shows such typical values of k_{ref} that we calculated with Equation 33 for a range of values of v_F and dP/dL. Some studies could estimate values of v_F and dP/dL for natural (de)hydration zones. For example, Beinlich et al. (2020) studied a ~2.6 m thick reaction zone in which serpentinite was replaced by soapstone (a talc-magnesite-chlorite assemblage). This replacement proceeded as a coupled carbonation and partial dehydration reaction (Beinlich et al., 2020) and the reaction is, hence, slightly more complex than the serpentinite dehydration considered in our model. Beinlich et al. (2020) estimated the duration for the generation of the 2.6 m thick zone to range between 15 and 29 years, which provides average propagation velocities, v_F, between 9 and 17 cm/yr. They further assume a pressure gradient driving the fluid flow of ~0.019 MPa/m which is controlled by the difference between fluid and solid densities. In our model, the calculated pressure represents the difference between the fluid pressure and ambient total pressure and, hence, represents a fluid overpressure of the form $P_f - P$ (see also Equation 19). Hydration requires a positive fluid overpressure while dehydration requires a negative fluid overpressure, or fluid underpressure. The fluid overpressure is likely limited by the tensile strength of rocks which is typically in the order of 10 MPa (e.g., Perras & Diederichs, 2014). Using 10 MPa as the maximum value for P_c yields for the 2.6 m wide reaction zone a value of $dP/dL \approx 4$ MPa/m. Values of dP/dL between 0.019 and 4 MPa/m and v_F between 9 and 17 cm/yr provide estimates of permeabilities, k_{ref}, between 10^{-20} and 10^{-18} m^2 (blue dashed rectangle in Figure 14). These
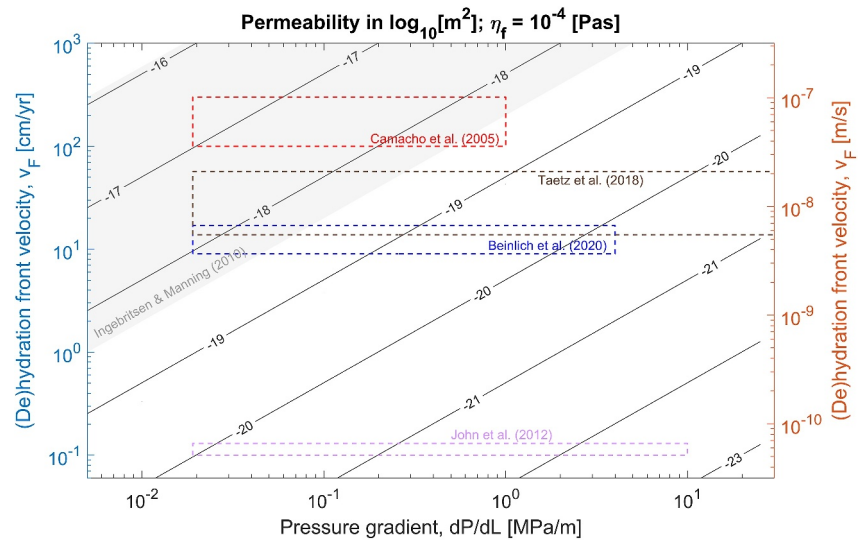
Figure 14. Estimates of permeabilities as a function of pressure gradient, dP/dL, and (de)hydration front velocity, v_F (Equation 33). The left vertical axis indicates v_F in units of cm/yr and the right axis in m/s. The fluid viscosity $\eta_f = 10^{-4}$ Pas. The gray region shows the range of typical permeabilities in the ductile crust at depths <10 km (Ingebritsen & Manning, 2010). The colored dashed rectangles indicate the range of estimates of dP/dL and v_F for observed reaction zones described in the respective references displayed in the same color (see Section 5.7).

permeabilities agree with typical permeabilities for ductile crustal rock (Figure 14). To provide a sharp reaction front, the permeability of the serpentinite should be smaller than the permeability of the produced soapstone through which the fluid flows. Therefore, we expect that the permeability of the serpentinite should have been significantly smaller than 10^{-20} m^2 at the lithostatic pressure of ∼3 kbar (Beinlich et al., 2020) at which the fluid infiltration occurred. Katayama et al. (2012) measured the permeabilities of serpentinite at low confining pressures of 50 MPa and obtained values between 10^{-21} and 10^{-20} m^2. Hatakayama et al. (2017) propose that the serpentinite permeability can be smaller than 10^{-21} m^2 for a lithostatic pressure of 3 kbar. Therefore, the serpentinite permeability was likely ∼10^{-21} m^2, or even smaller, and, hence, significantly smaller than 10^{-20} m^2. Consequently, a sharp reaction front between produced soapstone and reacted serpentinite could have been generated and propagated by a mechanism like the one described in our mathematical hydration model.

Another potential application of our model is the eclogitization of granulite studied by Camacho et al. (2005). They investigated eclogite lenses with dimensions between 10 and 30 m in granulite and proposed that the duration of fluid injection, causing the eclogitization, was less than 10 years. Using values between 10 and 30 m as representative values of L, and values between 5 and 10 years as representative values of t_c provides values of v_F between 1 and 3 m/yr. Assuming again 10 MPa as maximum value of P_c provides a maximum value of $dP/dL = 1$ MPa/m for $L = 10$ m. As minimum value for dP/dL we assume again 0.019 MPa/m. These estimates for v_F and dP/dL provide permeability estimates between $10^{-18.5}$ and 10^{-17} m^2 (red dashed rectangle in Figure 14). These permeability estimates again agree with typical deeper crustal permeabilities (Figure 14).

Our permeability estimates are based on models that assume that (de)hydration front propagation is controlled by advection due to porous fluid flow. Generally, (de)hydration front propagation can be controlled by advection or diffusion, or by a combination of both processes whereby advection and diffusion have approximately equal importance (e.g., Ague, 2014; Bickle & McKenzie, 1987; Fletcher & Hofmann, 1974). Two case studies by John et al. (2012), for a dehydration zone in the Chinese Tianshan Mountains, and Taetz et al. (2018), for a dehydration zone in the Pouébo Eclogite Mélange, New Caledonia, used lithium-diffusion modeling to estimate the duration of dehydration pulses during subduction. For these two case studies, diffusion is required to explain the observed lithium fractionation taking place on the time scale of the dehydration. Hence, John et al. (2012) and Taetz et al. (2018) assume dehydration front propagation was diffusion-controlled. Nevertheless, advection could have contributed to the propagation of these dehydration fronts. However, if advection contributed to dehydration front propagation, the advection velocity was limited by the duration constrained by the observed lithium fractionation. In other words, the maximal advection velocity is determined by the thickness of the dehydration front and the

diffusion-controlled duration of dehydration. We estimate the permeability for these two case studies with our method to constrain an upper bound on the transient permeability. Natural permeabilities could not have been higher than the maximum permeabilities estimated with our method, because otherwise, the dehydration zone would have developed too fast so that the observed lithium fractionation would not have had enough time to develop. John et al. (2012) and recalculations with updated partition coefficients and porosity data by Taetz et al. (2018) estimated a dehydration duration of approximately 760 years (we use here the range 760–1,000 years) for an approximately 1 m thick zone. Taetz et al. (2018) estimated a dehydration duration between 0.07 and 0.29 years for a zone with approximately 4 cm thickness. To estimate a maximum value of dP/dL we assume again 10 MPa as maximum difference across the dehydration zone and we use again 0.019 MPa/m as minimum value for dP/dL. For the case of Taetz et al. (2018) the maximum permeability estimate is $\sim 5 \times 10^{-18}$ m^2 and for John et al. (2012) $\sim 10^{-20}$ m^2 (Figure 14). We suggest that these maximum permeability estimates represent upper bounds for natural, reaction-induced permeability for the two respective case studies.

6. Conclusions

We present a 1D HMC model that predicts the propagation of hydration and dehydration fronts. We consider reactions for which the solid density of the reactants, such as serpentinite or granulite, is smaller than the solid density of the products, such as olivine or eclogite. Our models indicate that reactions can drive the propagation of (de)hydration fronts, characterized by sharp porosity fronts, into a viscous medium with zero permeability. Previous studies showed that in the absence of reactions porosity fronts cannot propagate into a viscous medium with zero permeability and get trapped. Therefore, reactions and the associated transient, reaction-induced porosity likely play a key role in the natural migration of fluids across viscous regions with very low background permeability, such as the mantle wedge, the deeper regions of the lithosphere, or the lower crust.

We present an analytical expression for the transient, reaction-induced porosity generated by (de)hydration reactions. This porosity depends on (a) changes in solid density, (b) changes in the mass fraction of structurally bound water, and (c) solid volumetric deformation. We show that this porosity expression can be used to numerically simulate (de)hydration front propagation into a medium with zero initial porosity.

Our numerical simulations confirm the proposed hypothesis for three different (de)hydration scenarios: (a) hydration with an inflow of external fluid, (b) dehydration with an outflow of the liberated fluid, and (c) dehydration-inflow for which despite fluid liberation additional external fluid flows into the reaction-induced porosity. A representative reaction for the hydration scenario is the hydration (eclogitization) of granulite, for the dehydration scenario the dehydration of serpentinite (brucite-out) at conditions for which the Clapeyron slope is positive, and for the dehydration-inflow scenario the dehydration of serpentinite (antigorite-out) at conditions for which the Clapeyron slope is negative. Fluid pressure gradients control fluid flow and fluid flows from higher to lower fluid pressure. Therefore, the fluid flow direction is governed by the positioning of the free fluid phase in the pressure-temperature phase diagram. If the free fluid phase resides above the reaction pressure, the fluid can flow in the same direction as a propagating hydration or dehydration front. Conversely, if the free fluid phase sits below the reaction pressure, the fluid flows away from a propagating dehydration front. The positioning of the free fluid phase is governed by the change of solid density across the reaction boundary. If the solid density increases for a pressure increase across the reaction boundary, the free fluid phase is located above the reaction pressure, favoring the propagation of both hydration and dehydration fronts. Conversely, if the solid density decreases for a pressure increase across the reaction boundary the free fluid phase is located below the reaction pressure, favoring only the propagation of dehydration fronts. For the zero-porosity limit, mass transport by fluid flow is guaranteed because the chemical signal in the fluid propagates with the same velocity as the porosity front.

Estimating transient, reaction-induced permeabilities associated with the propagation of natural (de)hydration fronts is challenging. We propose a new method to estimate reaction-induced permeabilities which can be applied if estimates for the duration of (de)hydration and fluid pressure gradients are available. We estimate reaction-induced permeabilities for natural (de)hydration zones and obtain permeability values like those suggested for deep crustal and subduction zone conditions based on other methods.

Appendix A: Porosity Change Due To Reaction and Solid Deformation

Here, we show the steps to transform Equations 21 into 23. Applying the product rule of differentiation to the right-hand side of Equation 21 and moving the term multiplied by v_s to the left-hand side yields
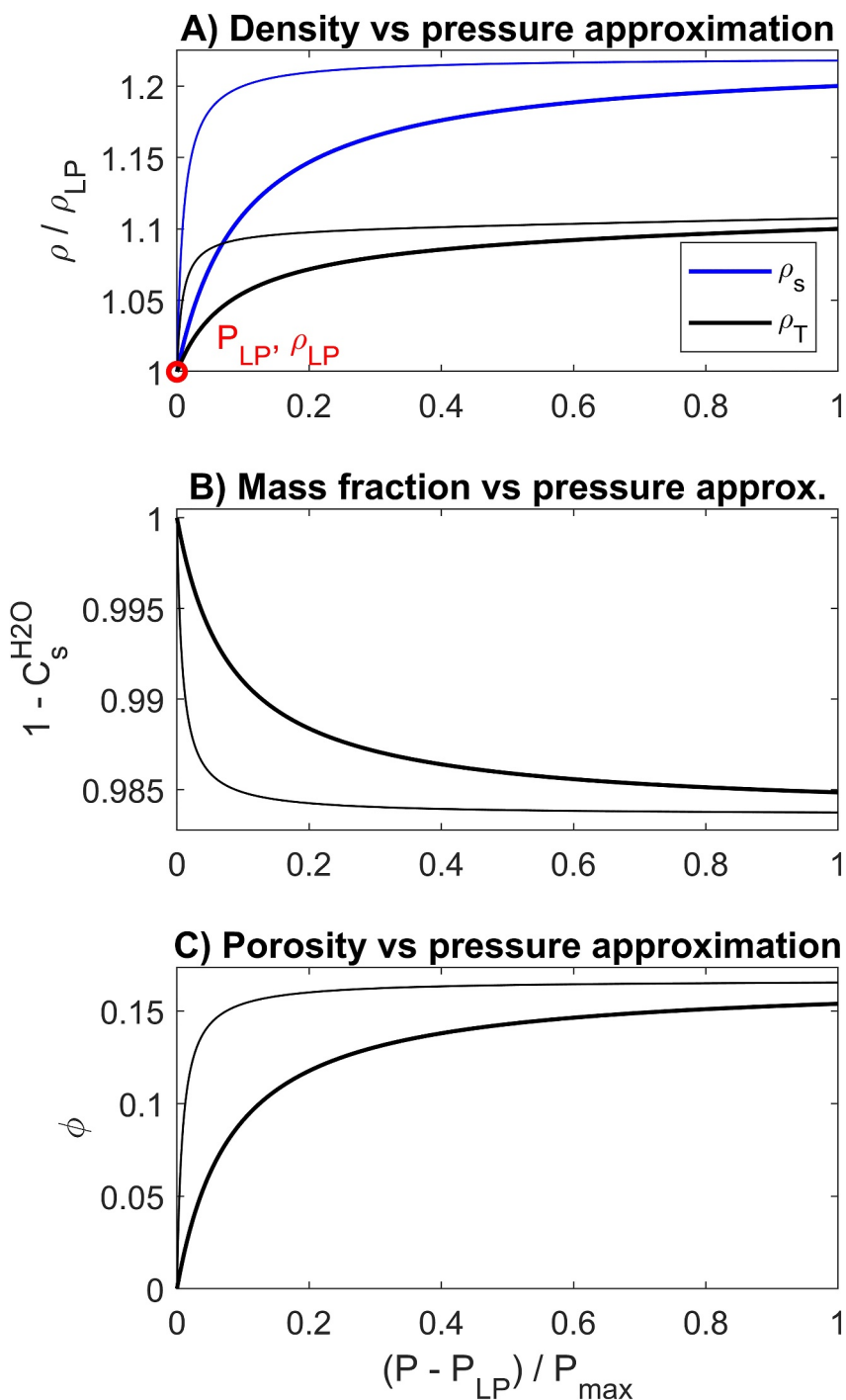
Figure A1. Applied limits of the parameterized relationships of densities (a), mass fraction (b) and porosity (c) versus pressure applied in the systematic numerical simulations for hydration which were used to generate Figure 13. The thicker lines correspond to $\Delta P_f = 0.1$ and the thinner lines to $\Delta P_f = 0.01$. The value of ΔP_f controls the sharpness of the reaction (see vertical axis of Figure 13). Symbols are explained in Table 1.

$$\frac{\partial}{\partial t}\big(\rho_s(1-\phi)\big(1-C_s^{H_2O}\big)\big) + v_s\frac{\partial}{\partial x}\big(\rho_s(1-\phi)\big(1-C_s^{H_2O}\big)\big) = -\rho_s(1-\phi)\big(1-C_s^{H_2O}\big)\frac{\partial}{\partial x}(v_s) \qquad (A1)$$

The term on the left-hand side, which is multiplied by v_s, represents an advection term for the quantity $\rho_s(1-\phi)\big(1-C_s^{H_2O}\big)$. The left-hand side can, hence, be combined to the total time derivative, d/dt, of $\rho_s(1-\phi)\big(1-C_s^{H_2O}\big)$ and both sides of the equation can be divided by $\rho_s(1-\phi)\big(1-C_s^{H_2O}\big)$ to yield

$$\frac{1}{\rho_s(1-\phi)\big(1-C_s^{H_2O}\big)}\frac{d}{dt}\big(\rho_s(1-\phi)\big(1-C_s^{H_2O}\big)\big) = -\frac{\partial}{\partial x}(v_s) \qquad (A2)$$

The left-hand side can now be replaced by the time derivative of the natural logarithm of $\rho_s(1-\phi)\big(1-C_s^{H_2O}\big)$ and the right-hand side can be modified by using Equation 22 to yield

$$\frac{d}{dt}\ln\big(\rho_s(1-\phi)\big(1-C_s^{H_2O}\big)\big) = -\frac{d}{dt}\ln V \qquad (A3)$$

All terms can be combined on the left-hand side of the equation inside the total time derivative and using the product rule for logarithms yields (Khakimova & Podladchikov, 2024):

$$\frac{d}{dt}\ln\big(\rho_s(1-\phi)\big(1-C_s^{H_2O}\big)V\big) = 0. \qquad (A4)$$

When the time derivative of the logarithm of a quantity that can change with time is equal to zero then the time derivative of this quantity must be equal to zero. Therefore, Equation A4 can be transformed into Equation 23.

Appendix B: Mass- and Molar-Based Porosity Calculations

A particular challenge when studying the literature on (de)hydration is that more chemically oriented studies commonly base their calculations for porosity and volume change on quantities with units involving moles (e.g., Centrella et al., 2015) while more physically oriented studies commonly base such calculations on quantities with units involving kilograms (e.g., Plümper et al., 2017). Several controversies and contradictory results, concerning typically the quantification of changes in porosity, volume, and pressure during metamorphic reactions, are often related to calculations based on either molar- or mass-based quantities (e.g., Hess et al., 2022; Powell et al., 2018; Tajčmanová et al., 2015, 2021). If the molar- and mass-based calculations are each internally consistent, then they must provide the same result for the same process because each calculation is based on the same fundamental laws of physics and thermodynamics. To show the consistency of our mathematical model, we discuss some results for porosity change during (de)hydration with both molar- and mass-based calculations and show that they are identical.

Equation 14 to calculate ϕ has been derived from general mass conservation equations involving densities and mass fractions. We refer to this approach to calculate ϕ as mass-based calculation. One advantage of the mass-based calculation is that no matter how many minerals are involved in a (de)hydration reaction, we need to use only one value of ρ_s and of $C_s^{H_2O}$ for each side of the reaction, because values of ρ_s and of $C_s^{H_2O}$ represent the entire rock, or mineral assemblage. However, in petrological studies, calculations of ϕ change during (de)hydration are frequently based on moles and molar volumes (e.g., Putnis, 2009). We show here that Equation 14 to calculate ϕ due to (de)hydration can be reformulated to alternatively calculate ϕ with molar-based quantities, such as molar volumes.

The calculation of ϕ with Equation 14 can be done with moles and molar volumes if the quantities ρ_{s0}, ρ_s, $C_{s0}^{H_2O}$, and $C_s^{H_2O}$ are expressed in moles and molar volumes. To do this, we introduce the parameters N_{s0}, N_s, $N_{s0}^{H_2O}$, and $N_s^{H_2O}$ which are the initial number of moles of solid components, the final number of moles of solid components, the initial number of moles of H_2O in the solid and the final number of moles of H_2O in the solid, respectively. For didactical reasons, we illustrate the parameters for the simple dehydration reaction:

$$\underset{\text{brucite}}{\text{Mg(OH)}_2} \rightarrow \underset{\text{periclase}}{\text{MgO}} + \underset{\text{water}}{\text{H}_2\text{O}}. \tag{B1}$$

Brucite is the initial solid and periclase the final solid. For this simple reaction we have only one solid component, namely MgO. Hence, for this reaction we have $N_{s0} = 1$, $N_s = 1$, $N_{s0}^{\text{H}_2\text{O}} = 1$, and $N_s^{\text{H}_2\text{O}} = 0$. Next, we introduce V_{s0}^{mol} and V_s^{mol} which are the initial (here brucite) and final (here periclase) molar volumes of the solid, respectively. The molar mass of the pure solid component, that is the component without structurally bound water, is termed here $M_{s\text{pure}}^{\text{mol}}$, which for the considered reaction is the periclase, MgO, component. In our models, the molar mass of the pure solid component does not change during the reaction, hence $M_{s0\text{pure}}^{\text{mol}} = M_{s\text{pure}}^{\text{mol}}$. The molar mass of water is termed $M_{\text{H}_2\text{O}}^{\text{mol}}$. The molar mass of the initial solid is then $M_{s0}^{\text{mol}} = N_{s0}M_{s0\text{pure}}^{\text{mol}} + N_{s0}^{\text{H}_2\text{O}}M_{\text{H2O}}^{\text{mol}}$ and of the final solid $M_s^{\text{mol}} = N_sM_{s\text{pure}}^{\text{mol}} + N_s^{\text{H}_2\text{O}}M_{\text{H2O}}^{\text{mol}}$. With the molar masses and the molar volumes, we can calculate the densities of the initial and final solids with $\rho_{s0} = M_{s0}^{\text{mol}}/V_{s0}^{\text{mol}}$ and $\rho_s = M_s^{\text{mol}}/V_s^{\text{mol}}$. The mass fraction of the solid component in the initial solid is $C_{s0} = N_{s0}M_{s0\text{pure}}^{\text{mol}}/M_{s0}^{\text{mol}}$ and in the final solid is $C_s = N_sM_{s\text{pure}}^{\text{mol}}/M_s^{\text{mol}}$. These two mass fractions are related to the mass fractions of H_2O which is structurally bound in the solid by the relations $C_{s0} = 1 - C_{s0}^{\text{H}_2\text{O}}$ and $C_s = 1 - C_s^{\text{H}_2\text{O}}$. We can now replace the densities and mass fractions in Equation 14 by their molar expressions given above and apply the relation $N_{s0} = N_s$, which yields

$$\phi = 1 - \frac{V_s^{\text{mol}}}{V_{s0}^{\text{mol}}}. \tag{B2}$$

At room temperature, $\rho_s \approx 2{,}380$ kg m^{-3} and $C_s = 1 - C_s^{\text{H}_2\text{O}} \approx 0.69$ for brucite, and $\rho_s \approx 3{,}585$ kg m^{-3} and $C_s = 1 - C_s^{\text{H}_2\text{O}} = 1$ for periclase. Using the mass-based calculation and assuming that brucite is the reactant, the initial rock, with $\phi_0 = 0$ and periclase is the product, Equation 14 provides $\phi = 1 - (2{,}380 \times 0.69/3{,}585) \approx 0.54$. Using the molar-based approach and employing $V_{s0}^{\text{mol}} = 24.63$ cm^3 for brucite and $V_s^{\text{mol}} = 11.248$ cm^3 for periclase yields $\phi = 1 - (11.248/24.63) \approx 0.54$. The mass- and molar-based porosity calculations yield, hence, the same results.

Next, we show the calculation of ϕ for the considered SOR. At room temperature, $\rho_s \approx 2{,}573$ kg m^{-3} and $C_s = 1 - C_s^{\text{H}_2\text{O}} \approx 0.84$ for the solid made of antigorite + brucite, and $\rho_s \approx 3{,}213$ kg m^{-3} and $C_s = 1 - C_s^{\text{H}_2\text{O}} = 1$ for forsterite. Using the mass-based calculation and assuming that the rock made of antigorite + brucite is the reactant with $\phi_0 = 0$ and forsterite is the product, Equation 14 provides $\phi = 1 - (2{,}573 \times 0.83/3{,}213) \approx 0.34$. The molar-based approach becomes more elaborated because we have to consider the stoichiometric coefficients for antigorite, $\nu_{s01} = 1$, brucite, $\nu_{s02} = 20$, and forsterite, $\nu_{s1} = 34$. The molar volumes of the minerals are $V_{s01}^{\text{mol}} = 1{,}754.8$ cm^3 for antigorite, $V_{s02}^{\text{mol}} = 24.63$ cm^3 for brucite and $V_{s1}^{\text{mol}} = 43.79$ cm^3 for forsterite. Following the same procedure as above, we can derive the equation for the porosity for the molar-based approach in the form:

$$\phi = 1 - \left(\frac{\nu_{s1}V_{s1}^{\text{mol}}}{(\nu_{s01}V_{s01}^{\text{mol}} + \nu_{s02}V_{s02}^{\text{mol}})} \right). \tag{B3}$$

Using the values for the stoichiometric coefficients and molar volumes yields $\phi = 1 - (34 \times 43.79/(1 \times 1{,}754.8 + 20 \times 24.63)) \approx 0.34$. Again, the mass- and molar-based approach provide the same values for porosities.

Appendix C: Thermodynamic Pressure

In a rock without porosity under a hydrostatic state of stress, the thermodynamic pressure is given by the mean stress of the rock (e.g., Moulas et al., 2019). In a porous rock involving differential stress, it is currently debated which pressure or stress magnitude should be used as magnitude for the thermodynamic pressure in the Gibbs equation, for example, fluid pressure, total mean stress or normal stress on crystalline interfaces (e.g., Moulas et al., 2019; Wheeler, 2014, 2018, 2020). This debate has minimal impact on our models as we do not consider deviatoric stress, and the assumed fluid over- and underpressure is small (<10 MPa). Hence, the fundamental

features of the coupling between reactions, fluid flow and solid deformation during (de)hydration would not change significantly for our models.

Appendix D: Systematic Hydration Simulations

In the systematic hydration simulations used to generate the results presented in Figure 13, we varied the porosity exponent, n, in the porosity-permeability relation and the parameter ΔP_f that controls the pressure interval over which the reaction occurs. The smaller the value of ΔP_f the sharper the change of the density, mass fraction, and porosity across the reaction boundary. The sharpest and smoothest parameterized density, mass fraction and porosity profiles for $\Delta P_f = 0.01$ and 0.1, respectively, which we used in the systematic simulations, are indicated in Figure A1.

Data Availability Statement

The numerical algorithm for the HC model III and the HMC model IV is openly accessible via Schmaste (2024).

References

Ague, J. J. (2014). 4.6—Fluid flow in the deep crust. In H. D. Holland, & K. K. Turekian (Eds.) *Treatise on geochemistry* (2nd ed., pp. 203–247). Elsevier. https://doi.org/10.1016/B978-0-08-095975-7.00306-5

Aharonov, E., Whitehead, J., Kelemen, P., & Spiegelman, M. (1995). Channeling instability of upwelling melt in the mantle. *Journal of Geophysical Research*, *100*(B10), 20433–20450. https://doi.org/10.1029/95jb01307

Austrheim, H. (1987). Eclogitization of lower crustal granulites by fluid migration through shear zones. *Earth and Planetary Science Letters*, *81*(2–3), 221–232. https://doi.org/10.1016/0012-821x(87)90158-0

Baïsset, M., Labrousse, L., Schubnel, A., Gasc, J., Béneut, K., & Guillaumet, M. (2024). Rheology of hydrated plagioclase at lower crustal conditions: Cataclasis, creep and transformational plasticity. *Journal of Structural Geology*, *178*, 105010. https://doi.org/10.1016/j.jsg.2023.105010

Barcilon, V., & Richter, F. M. (1986). Nonlinear waves in compacting media. *Journal of Fluid Mechanics*, *164*, 429–448. https://doi.org/10.1017/s0022112086002628

Barenblatt, G., Bertsch, M., Chertock, A., & Prostokishin, V. (2000). Self-similar intermediate asymptotics for a degenerate parabolic filtration-absorption equation. *Proceedings of the National Academy of Sciences*, *97*(18), 9844–9848. https://doi.org/10.1073/pnas.97.18.9844

Baumgartner, L. P., & Ferry, J. M. (1991). A model for coupled fluid-flow and mixed-volatile mineral reactions with applications to regional metamorphism. *Contributions to Mineralogy and Petrology*, *106*(3), 273–285. https://doi.org/10.1007/BF00324557

Beinlich, A., John, T., Vrijmoed, J., Tominaga, M., Magna, T., & Podladchikov, Y. (2020). Instantaneous rock transformations in the deep crust driven by reactive fluid flow. *Nature Geoscience*, *13*(4), 307–311. https://doi.org/10.1038/s41561-020-0554-9

Bessat, A., Pilet, S., Podladchikov, Y. Y., & Schmalholz, S. M. (2022). Melt migration and chemical differentiation by reactive porosity waves. *Geochemistry, Geophysics, Geosystems*, *23*(2). https://doi.org/10.1029/2021gc009963

Bhatnager, P. (1979). *Nonlinear waves in one-dimensional dispersive system* (Vol. 61, p. 88). Clarendon Press.

Bickle, M., & McKenzie, D. (1987). The transport of heat and matter by fluids during metamorphism. *Contributions to Mineralogy and Petrology*, *95*(3), 384–392. https://doi.org/10.1007/bf00371852

Biot, M. A. (1941). General theory of three-dimensional consolidation. *Journal of Applied Physics*, *12*(February), 155–164. https://doi.org/10.1063/1.1712886

Biot, M. A. (1962). Generalized theory of acoustic propagation in porous dissipative media. *Journal of the Acoustical Society of America*, *34*(9), 1254. https://doi.org/10.1121/1.1918315

Biot, M. A., & Willis, D. G. (1957). The elastic coefficients of the theory of consolidation.

Brantut, N., Schubnel, A., David, E. C., Héripré, E., Guéguen, Y., & Dimanov, A. (2012). Dehydration-induced damage and deformation in gypsum and implications for subduction zone processes. *Journal of Geophysical Research*, *117*(B3), 3205. https://doi.org/10.1029/2011JB008730

Bras, E., Yamato, P., Schmalholz, S. M., Duretz, T., & Podladchikov, Y. Y. (2023). Eclogitisation of dry and impermeable granulite by fluid flow with reaction-induced porosity: Insights from hydro-chemical modelling. *Earth and Planetary Science Letters*, *617*, 118256. https://doi.org/10.1016/j.epsl.2023.118256

Cagnioncle, A. M., Parmentier, E., & Elkins-Tanton, L. T. (2007). Effect of solid flow above a subducting slab on water distribution and melting at convergent plate boundaries. *Journal of Geophysical Research*, *112*(B9), B09402. https://doi.org/10.1029/2007jb004934

Callen, H. B. (1998). *Thermodynamics and an introduction to thermostatistics*. American Association of Physics Teachers.

Camacho, A., Lee, J. K., Hensen, B. J., & Braun, J. (2005). Short-lived orogenic cycles and the eclogitization of cold crust by spasmodic hot fluids. *Nature*, *435*(7046), 1191–1196. https://doi.org/10.1038/nature03643

Carman, P. C. (1937). Fluid flow through granular beds. *Chemical Engineering Research and Design*, *75*, S32–S48. https://doi.org/10.1016/s0263-8762(97)80003-2

Centrella, S. (2019). The granulite-to eclogite-and amphibolite-facies transition: A volume and mass transfer study in the Lindås Nappe, Bergen arcs, west Norway. *Geological Society, London, Special Publications*, *478*(1), 241–264. https://doi.org/10.1144/sp478.9

Centrella, S., Austrheim, H., & Putnis, A. (2015). Coupled mass transfer through a fluid phase and volume preservation during the hydration of granulite: An example from the Bergen Arcs, Norway. *Lithos*, *236*, 245–255. https://doi.org/10.1016/j.lithos.2015.09.010

Chakraborty, S. (2017). A new mechanism for upper crustal fluid flow driven by solitary porosity waves in rigid reactive media? *Geophysical Research Letters*, *44*(20), 10324–10327. https://doi.org/10.1002/2017gl075798

Chorin, A. J. (1997). A numerical method for solving incompressible viscous flow problems. *Journal of Computational Physics*, *135*(2), 118–125. https://doi.org/10.1006/jcph.1997.5716

Connolly, J. A. D. (2005). Computation of phase equilibria by linear programming: A tool for geodynamic modeling and its application to subduction zone decarbonation. *Earth and Planetary Science Letters*, *236*(1–2), 524–541. https://doi.org/10.1016/j.epsl.2005.04.033

Connolly, J. A. D., & Podladchikov, Y. Y. (1998). Compaction-driven fluid flow in viscoelastic rock. *Geodinamica Acta*, *11*(2–3), 55–84. https://doi.org/10.1016/s0985-3111(98)80006-5

Connolly, J. A. D., & Podladchikov, Y. Y. (2007). Decompaction weakening and channeling instability in ductile porous media: Implications for asthenospheric melt segregation. *Journal of Geophysical Research*, *112*, B10. https://doi.org/10.1029/2005jb004213

Connolly, J. A. D., & Podladchikov, Y. Y. (2015). An analytical solution for solitary porosity waves: Dynamic permeability and fluidization of nonlinear viscous and viscoplastic rock. *Geofluids*, *15*(1–2), 269–292. https://doi.org/10.1111/gfl.12110

Coussy, O. (2004). *Poromechanics*. John Wiley & Sons.

Dahlen, F. A. (1992). Metamorphism of nonhydrostatically stressed rocks. *American Journal of Science*, *292*(3), 184–198. https://doi.org/10.2475/ajs.292.3.184

Darcy, H. (1856). Les fontaines publiques de la ville de Dijon: exposition et application des principes à suivre et des formules à employer dans les questions de distribution d'eau… un appendice relatif aux fournitures d'eau de plusieurs villes au filtrage des eaux, Victor Dalmont, éditeur.

De Groot, S. R., & Mazur, P. (1984). *Non-equilibrium thermodynamics*. Courier Corporation.

Evans, B. W. (2004). The serpentinite multisystem revisited: Chrysotile is metastable. *International Geology Review*, *46*(6), 479–506. https://doi.org/10.2747/0020-6814.46.6.479

Evans, O., Spiegelman, M., & Kelemen, P. B. (2018). A poroelastic model of serpentinization: Exploring the interplay between rheology, surface energy, reaction, and fluid flow. *Journal of Geophysical Research: Solid Earth*, *123*(10), 8653–8675. https://doi.org/10.1029/2017jb015214

Evans, O., Spiegelman, M., & Kelemen, P. B. (2020). Phase-field modeling of reaction-driven cracking: Determining conditions for Extensive olivine serpentinization. *Journal of Geophysical Research: Solid Earth*, *125*(1), e2019JB018614. https://doi.org/10.1029/2019jb018614

Ferrand, T. P., Hilairet, N., Incel, S., Deldicque, D., Labrousse, L., Gasc, J., et al. (2017). Dehydration-driven stress transfer triggers intermediate-depth earthquakes. *Nature Communications*, *8*(1), 15247. https://doi.org/10.1038/ncomms15247

Fletcher, R., & Hofmann, A. (1974). Simple models of diffusion and combined diffusion-infiltration metasomatism. In *Geochemical transport and kinetics* (pp. 243–259). Carnegie Institution of Washington.

Frolov, T., & Mishin, Y. (2010). Effect of nonhydrostatic stresses on solid-fluid equilibrium. I. Bulk thermodynamics. *Physical Review B*, *82*(17), 174113. https://doi.org/10.1103/physrevb.82.174113

Gerya, T. V. (2019). *Introduction to numerical geodynamic modelling*. Cambridge University Press.

Gerya, T. V., & Meilick, F. I. (2011). Geodynamic regimes of subduction under an active margin: Effects of rheological weakening by fluids and melts. *Journal of Metamorphic Geology*, *29*(1), 7–31. https://doi.org/10.1111/j.1525-1314.2010.00904.x

Ghorbani, J., Nazem, M., & Carter, J. (2016). Numerical modelling of multiphase flow in unsaturated deforming porous media. *Computers and Geotechnics*, *71*, 195–206. https://doi.org/10.1016/j.compgeo.2015.09.011

Gibbs, J. W. (1906). *On the equilibrium of heterogeneous substances: The scientific papers of J. Willard Gibbs*. Longmans.

Gray, W. G., & O'Neill, K. (1976). On the general equations for flow in porous media and their reduction to Darcy's law. *Water Resources Research*, *12*(2), 148–154. https://doi.org/10.1029/wr012i002p00148

Griggs, D., & Blacic, J. (1965). Quartz: Anomalous weakness of synthetic crystals. *Science*, *147*(3655), 292–295. https://doi.org/10.1126/science.147.3655.292

Grove, T. L., Chatterjee, N., Parman, S. W., & Múdard, E. (2006). The influence of H_2O on mantle wedge melting. *Earth and Planetary Science Letters*, *249*(1–2), 74–89. https://doi.org/10.1016/j.epsl.2006.06.043

Guy, B. (1993). Mathematical revision of Korzhinskii's theory of infiltration metasomatic zoning. *European Journal of Mineralogy*, *5*(2), 317–339. https://doi.org/10.1127/ejm/5/2/0317

Hacker, B. R., Kelemen, P. B., & Behn, M. D. (2015). Continental lower crust. *Annual Review of Earth and Planetary Sciences*, *43*(1), 167–205. https://doi.org/10.1146/annurev-earth-050212-124117

Hatakeyama, K., Katayama, I., Hirauchi, K.-I., & Michibayashi, K. (2017). Mantle hydration along outer-rise faults inferred from serpentinite permeability. *Scientific Reports*, *7*(1), 13870. https://doi.org/10.1038/s41598-017-14309-9

Heard, H. C., & Rubey, W. W. (1966). Tectonic implications of gypsum dehydration. *GSA Bulletin*, *77*(7), 741–760. https://doi.org/10.1130/0016-7606(1966)77[741:Tiogd]2.0.Co;2

Hermann, J., Müntener, O., & Scambelluri, M. (2000). The importance of serpentinite mylonites for subduction and exhumation of oceanic crust. *Tectonophysics*, *327*(3–4), 225–238. https://doi.org/10.1016/s0040-1951(00)00171-2

Hess, B. L., Ague, J. J., & Voorhees, P. W. (2022). Quantifying the effects of non-hydrostatic stress on multi-component minerals. *Journal of Geophysical Research: Solid Earth*, *127*(9), e2022JB025201. https://doi.org/10.1029/2022jb025201

Hobbs, B., & Ord, A. (2015). *Structural Geology—The mechanics of deforming metamorphic rocks* (p. 680). Elsevier. https://doi.org/10.1016/C2012-0-01215-X

Hu, H., Jackson, M. D., & Blundy, J. (2022). Melting, compaction and reactive flow: Controls on melt fraction and composition change in crustal mush reservoirs. *Journal of Petrology*, *63*(11), egac097. https://doi.org/10.1093/petrology/egac097

Huber, K., Vrijmoed, J. C., & John, T. (2022). Formation of olivine veins by reactive fluid flow in a dehydrating serpentinite. *Geochemistry, Geophysics, Geosystems*, *23*(6), e2021GC010267. https://doi.org/10.1029/2021gc010267

Huppert, H. E. (1982). The propagation of two-dimensional and axisymmetric viscous gravity currents over a rigid horizontal surface. *Journal of Fluid Mechanics*, *121*(1), 43–58. https://doi.org/10.1017/s0022112082001797

Hutter, K. (2017). *Theoretical glaciology: Material science of ice and the mechanics of glaciers and ice sheets*. Springer.

Ingebritsen, S. E., & Manning, C. (2010). Permeability of the continental crust: Dynamic variations inferred from seismicity and metamorphism. *Geofluids*, *10*(1–2), 193–205. https://doi.org/10.1111/j.1468-8123.2010.00278.x

John, T., Gussone, N., Podladchikov, Y. Y., Bebout, G. E., Dohmen, R., Halama, R., et al. (2012). Volcanic arcs fed by rapid pulsed fluid flow through subducting slabs. *Nature Geoscience*, *5*(7), 489–492. https://doi.org/10.1038/ngeo1482

Jones, D. W. R., & Katz, R. F. (2018). Reaction-infiltration instability in a compacting porous medium. *Journal of Fluid Mechanics*, *852*, 5–36. https://doi.org/10.1017/jfm.2018.524

Jordan, J. S., Hesse, M. A., & Rudge, J. F. (2018). On mass transport in porosity waves. *Earth and Planetary Science Letters*, *485*, 65–78. https://doi.org/10.1016/j.epsl.2017.12.024

Jung, H., Green Ii, H. W., & Dobrzhinetskaya, L. F. (2004). Intermediate-depth earthquake faulting by dehydration embrittlement with negative volume change. *Nature*, *428*(6982), 545–549. https://doi.org/10.1038/nature02412

Kaatz, L., Reynes, J., Hermann, J., & John, T. (2022). How fluid infiltrates dry crustal rocks during progressive eclogitization and shear zone formation: Insights from H2O contents in nominally anhydrous minerals. *Contributions to Mineralogy and Petrology*, *177*(7), 72. https://doi.org/10.1007/s00410-022-01938-1

Kaatz, L., Schmalholz, S., & John, T. (2023). Numerical simulations reproduce field observations showing transient weakening during shear zone formation by diffusional hydrogen influx and H$_2$O inflow. *Geochemistry, Geophysics, Geosystems*, *24*(5), e2022GC010830. https://doi.org/10.1029/2022gc010830

Kalashnikov, A. S. (1987). Some problems of the qualitative theory of non-linear degenerate second-order parabolic equations. *Russian Mathematical Surveys*, *42*(2), 169–222. https://doi.org/10.1070/rm1987v042n02abeh001309

Karato, S. (2008). *Deformation of Earth materials*. Cambridge University Press.

Katayama, I., Terada, T., Okazaki, K., & Tanikawa, W. (2012). Episodic tremor and slow slip potentially linked to permeability contrasts at the Moho. *Nature Geoscience*, *5*(10), 731–734. https://doi.org/10.1038/ngeo1559

Katz, R. F. (2008). Magma dynamics with the enthalpy method: Benchmark solutions and magmatic focusing at mid-ocean ridges. *Journal of Petrology*, *49*(12), 2099–2121. https://doi.org/10.1093/petrology/egn058

Kelemen, P. B., & Hirth, G. (2012). Reaction-driven cracking during retrograde metamorphism: Olivine hydration and carbonation. *Earth and Planetary Science Letters*, *345*, 81–89. https://doi.org/10.1016/j.epsl.2012.06.018

Keller, T., & Suckale, J. (2019). A continuum model of multi-phase reactive transport in igneous systems. *Geophysical Journal International*, *219*(1), 185–222. https://doi.org/10.1093/gji/ggz287

Khakimova, L., & Podladchikov, Y. (2024). Modeling multicomponent fluid flow in deforming and reacting porous rock. *Petrology*, *32*(1), 2–15. https://doi.org/10.1134/S0869591124010053

Klein, F., & Garrido, C. J. (2011). Thermodynamic constraints on mineral carbonation of serpentinized peridotite. *Lithos*, *126*(3–4), 147–160. https://doi.org/10.1016/j.lithos.2011.07.020

Koehn, D., Piazolo, S., Beaudoin, N. E., Kelka, U., Spruženiece, L., Putnis, C. V., & Toussaint, R. (2021). Relative rates of fluid advection, elemental diffusion and replacement govern reaction front patterns. *Earth and Planetary Science Letters*, *565*, 116950. https://doi.org/10.1016/j.epsl.2021.116950

Kozeny, J. (1927). Ueber kapillare leitung des wassers im boden. In *Sitzungsberichte der Akademie der Wissenschaften in Wien* (Vol. 136, p. 271).

Kuiken, G. D. (1994). *Thermodynamics of irreversible processes: Applications to diffusion and rheology*. Wiley.

Kuleci, H., Schmidt, C., Rybacki, E., Petrishcheva, E., & Abart, R. (2016). Hydration of periclase at 350°C to 620°C and 200 MPa: Experimental calibration of reaction rate. *Mineralogy and Petrology*, *110*(1), 1–10. https://doi.org/10.1007/s00710-015-0414-2

Kuleci, H., Ulven, O., Rybacki, E., Wunder, B., & Abart, R. (2017). Reaction-induced fracturing in a hot pressed calcite-periclase aggregate. *Journal of Structural Geology*, *94*, 116–135. https://doi.org/10.1016/j.jsg.2016.11.009

Kümpel, H.-J. (1991). Poroelasticity: Parameters reviewed. *Geophysical Journal International*, *105*(3), 783–799. https://doi.org/10.1111/j.1365-246X.1991.tb00813.x

Lacinska, A. M., Styles, M. T., Bateman, K., Hall, M., & Brown, P. D. (2017). An experimental study of the carbonation of serpentinite and partially serpentinised peridotites. *Frontiers in Earth Science*, *5*, 37. https://doi.org/10.3389/feart.2017.00037

Landau, L. D., & Lifshitz, E. M. (1980). *Statistical physics* (Vol. 5). Pergamon Press.

Lebon, G., Jou, D., & Casas-Vázquez, J. (2008). *Understanding non-equilibrium thermodynamics*. Springer.

Leclère, H., Faulkner, D., Llana-Fúnez, S., Bedford, J., & Wheeler, J. (2018). Reaction fronts, permeability and fluid pressure development during dehydration reactions. *Earth and Planetary Science Letters*, *496*, 227–237. https://doi.org/10.1016/j.epsl.2018.05.005

Lindgren, W. (1912). The nature of replacement. *Economic Geology*, *7*(6), 521–535. https://doi.org/10.2113/gsecongeo.7.6.521

Liu, J., Taylor, S. D., Qafoku, O., Arey, B. W., Colby, R., Eaton, A., et al. (2022). Visualizing the distribution of water in nominally anhydrous minerals at the atomic scale: Insights from atom probe tomography on fayalite. *Geophysical Research Letters*, *49*(2), e2021GL094914. https://doi.org/10.1029/2021gl094914

Llana-Fúnez, S., Wheeler, J., & Faulkner, D. R. (2012). Metamorphic reaction rate controlled by fluid pressure not confining pressure: Implications of dehydration experiments with gypsum. *Contributions to Mineralogy and Petrology*, *164*(1), 69–79. https://doi.org/10.1007/s00410-012-0726-8

Mahaffy, M. (1976). A three-dimensional numerical model of ice sheets: Tests on the Barnes Ice Cap, Northwest Territories. *Journal of Geophysical Research*, *81*(6), 1059–1066. https://doi.org/10.1029/jc081i006p01059

Malvern, L. E. (1969). Introduction to the mechanics of a continuous medium.

Malvoisin, B., Brunet, F., Carlut, J., Rouméjon, S., & Cannat, M. (2012). Serpentinization of oceanic peridotites: 2. Kinetics and processes of San Carlos olivine hydrothermal alteration. *Journal of Geophysical Research*, *117*(B4), B04102. https://doi.org/10.1029/2011JB008842

Malvoisin, B., Podladchikov, Y. Y., & Myasnikov, A. V. (2021). Achieving complete reaction while the solid volume increases: A numerical model applied to serpentinisation. *Earth and Planetary Science Letters*, *563*, 116859. https://doi.org/10.1016/j.epsl.2021.116859

Malvoisin, B., Podladchikov, Y. Y., & Vrijmoed, J. C. (2015). Coupling changes in densities and porosity to fluid pressure variations in reactive porous fluid flow: Local thermodynamic equilibrium. *Geochemistry, Geophysics, Geosystems*, *16*(12), 4362–4387. https://doi.org/10.1002/2015gc006019

Marti, S., Fusseis, F., Butler, I. B., Schlepütz, C., Marone, F., Gilgannon, J., et al. (2021). Time-resolved grain-scale 3D imaging of hydrofracturing in halite layers induced by gypsum dehydration and pore fluid pressure buildup. *Earth and Planetary Science Letters*, *554*, 116679. https://doi.org/10.1016/j.epsl.2020.116679

Mase, G. E. (1970). *Continuum mechanics*. McGraw-Hill.

Massonne, H.-J. (2009). Hydration, dehydration, and melting of metamorphosed granitic and dioritic rocks at high-and ultrahigh-pressure conditions. *Earth and Planetary Science Letters*, *288*(1–2), 244–254. https://doi.org/10.1016/j.epsl.2009.09.028

Mazzucchelli, M. L., Moulas, E., Kaus, B. J., & Speck, T. (2024). Fluid-mineral equilibrium under nonhydrostatic stress: Insight from molecular dynamics. *American Journal of Science*, *324*, 2. https://doi.org/10.2475/001c.92881

McKenzie, D. (1984). The generation and compaction of partially molten rock. *Journal of Petrology*, *25*(3), 713–765. https://doi.org/10.1093/petrology/25.3.713

Moulas, E., Schmalholz, S. M., Podladchikov, Y., Tajčmanová, L., Kostopoulos, D., & Baumgartner, L. (2019). Relation between mean stress, thermodynamic, and lithostatic pressure. *Journal of Metamorphic Geology*, *37*(1), 1–14. https://doi.org/10.1111/jmg.12446

Müller, I. (2007). *A history of thermodynamics: The doctrine of energy and entropy*. Springer Science & Business Media.

Ohtani, E. (2021). Hydration and dehydration in Earth's interior. *Annual Review of Earth and Planetary Sciences*, *49*(1), 253–278. https://doi.org/10.1146/annurev-earth-080320-062509

Omlin, S., Malvoisin, B., & Podladchikov, Y. Y. (2017). Pore fluid extraction by reactive solitary waves in 3-D. *Geophysical Research Letters*, *44*(18), 9267–9275. https://doi.org/10.1002/2017gl074293

Orr, F. M. (2007). *Theory of gas injection processes*. Tie-Line Publications Copenhagen.

Padrón-Navarta, J. A., Sánchez-Vizcaíno, V. L., Hermann, J., Connolly, J. A., Garrido, C. J., Gómez-Pugnaire, M. T., & Marchesi, C. (2013). Tschermak's substitution in antigorite and consequences for phase relations and water liberation in high-grade serpentinites. *Lithos*, *178*, 186–196. https://doi.org/10.1016/j.lithos.2013.02.001

Panfilov, M. (2018). Physicochemical fluid dynamics in porous media: Applications. In *Geosciences and petroleum engineering*. John Wiley & Sons.

Patankar, S. (2018). *Numerical heat transfer and fluid flow*. Taylor & Francis.

Peacock, S. M. (1990). Fluid processes in subduction zones. *Science*, *248*(4953), 329–337. https://doi.org/10.1126/science.248.4953.329

Perras, M. A., & Diederichs, M. S. (2014). A review of the tensile strength of rock: Concepts and testing. *Geotechnical & Geological Engineering*, *32*(2), 525–546. https://doi.org/10.1007/s10706-014-9732-0

Pesavento, F., Schrefler, B. A., & Sciumè, G. (2017). Multiphase flow in deforming porous media: A review. *Archives of Computational Methods in Engineering*, *24*(2), 423–448. https://doi.org/10.1007/s11831-016-9171-6

Philpotts, A. R., & Ague, J. J. (2022). *Principles of igneous and metamorphic petrology* (3rd ed.). Cambridge University Press.

Picazo, S., Malvoisin, B., Baumgartner, L., & Bouvier, A.-S. (2020). Low temperature serpentinite replacement by carbonates during seawater influx in the Newfoundland Margin. *Minerals*, *10*(2), 184. https://doi.org/10.3390/min10020184

Plümper, O., John, T., Podladchikov, Y. Y., Vrijmoed, J. C., & Scambelluri, M. (2017). Fluid escape from subduction zones controlled by channel-forming reactive porosity. *Nature Geoscience*, *10*(2), 150–156. https://doi.org/10.1038/ngeo2865

Plümper, O., Wallis, D., Teuling, F., Moulas, E., Schmalholz, S. M., Amiri, H., & Müller, T. (2022). High-magnitude stresses induced by mineral-hydration reactions. *Geology*, *50*(12), 1351–1355. https://doi.org/10.1130/g50493.1

Poulet, T., Veveakis, E., Regenauer-Lieb, K., & Yuen, D. (2014). Thermo-poro-mechanics of chemically active creeping faults: 3. The role of serpentinite in episodic tremor and slip sequences, and transition to chaos. *Journal of Geophysical Research: Solid Earth*, *119*(6), 4606–4625. https://doi.org/10.1002/2014jb011004

Powell, R., Evans, K. A., Green, E. C., & White, R. W. (2018). On equilibrium in non-hydrostatic metamorphic systems. *Journal of Metamorphic Geology*, *36*(4), 419–438. https://doi.org/10.1111/jmg.12298

Pride, S. R., & Berryman, J. G. (1998). Connecting theory to experiment in poroelasticity. *Journal of the Mechanics and Physics of Solids*, *46*(4), 719–747. https://doi.org/10.1016/s0022-5096(97)00043-4

Putnis, A. (2009). Mineral replacement reactions. *Reviews in Mineralogy and Geochemistry*, *70*(1), 87–124. https://doi.org/10.2138/rmg.2009.70.3

Putnis, A. (2021). Fluid–mineral interactions: Controlling coupled mechanisms of reaction, mass transfer and deformation. *Journal of Petrology*, *62*(12), egab092. https://doi.org/10.1093/petrology/egab092

Putnis, A., & John, T. (2010). Replacement processes in the Earth's crust. *Elements*, *6*(3), 159–164. https://doi.org/10.2113/gselements.6.3.159

Quinquis, M., & Buiter, S. (2014). Testing the effects of basic numerical implementations of water migration on models of subduction dynamics. *Solid Earth*, *5*(1), 537–555. https://doi.org/10.5194/se-5-537-2014

Ranero, C. R., Phipps Morgan, J., McIntosh, K., & Reichert, C. (2003). Bending-related faulting and mantle serpentinization at the Middle America trench. *Nature*, *425*(6956), 367–373. https://doi.org/10.1038/nature01961

Räss, L., Duretz, T., & Podladchikov, Y. (2019). Resolving hydromechanical coupling in two and three dimensions: Spontaneous channelling of porous fluids owing to decompaction weakening. *Geophysical Journal International*, *218*(3), 1591–1616. https://doi.org/10.1093/gji/ggz239

Räss, L., Utkin, I., Duretz, T., Omlin, S., & Podladchikov, Y. Y. (2022). Assessing the robustness and scalability of the accelerated pseudo-transient method. *Geoscientific Model Development*, *15*(14), 5757–5786. https://doi.org/10.5194/gmd-15-5757-2022

Roded, R., Paredes, X., & Holtzman, R. (2018). Reactive transport under stress: Permeability evolution in deformable porous media. *Earth and Planetary Science Letters*, *493*, 198–207. https://doi.org/10.1016/j.epsl.2018.04.041

Scambelluri, M., Cannaò, E., & Gilio, M. (2019). The water and fluid-mobile element cycles during serpentinite subduction: A review. *European Journal of Mineralogy*, *31*(3), 405–428. https://doi.org/10.1127/ejm/2019/0031-2842

Schiemenz, A., Liang, Y., & Parmentier, E. M. (2011). A high-order numerical study of reactive dissolution in an upwelling heterogeneous mantle-I. Channelization, channel lithology and channel geometry. *Geophysical Journal International*, *186*(2), 641–664. https://doi.org/10.1111/j.1365-246X.2011.05065.x

Schmalholz, S. M., Moulas, E., Plumper, O., Myasnikov, A. V., & Podladchikov, Y. Y. (2020). 2D hydro-mechanical-chemical modeling of (de)hydration reactions in deforming heterogeneous rock: The periclase-brucite model reaction. *Geochemistry, Geophysics, Geosystems*, *21*(11), e2020GC009351. https://doi.org/10.1029/2020gc009351

Schmalholz, S. M., Moulas, E., Räss, L., & Müntener, O. (2023). Serpentinite dehydration and olivine vein formation during ductile shearing: Insights from 2D numerical modeling on porosity generation, density variations, and transient weakening. *Journal of Geophysical Research: Solid Earth*, *128*(11), e2023JB026985. https://doi.org/10.1029/2023JB026985

Schmaste. (2024). schmaste/De-hydration: (De)hydration code (v1.0-dehydration_code_1D). *Zenodo*. https://doi.org/10.5281/zenodo.11129250

Schrank, C. E., Gaede, O., Blach, T., Gioseffi, K. C. M., Mudie, S., Kirby, N., et al. (2021). Fast in-situ X-ray scattering reveals stress sensitivity of gypsum dehydration kinetics. *Communications Materials*, *2*(1), 51. https://doi.org/10.1038/s43246-021-00156-9

Scott, D. R., & Stevenson, D. J. (1984). Magma solitons. *Geophysical Research Letters*, *11*(11), 1161–1164. https://doi.org/10.1029/gl011i011p01161

Scott, D. R., Stevenson, D. J., & Whitehead, J. A., Jr. (1986). Observations of solitary waves in a viscously deformable pipe. *Nature*, *319*(6056), 759–761. https://doi.org/10.1038/319759a0

Sekerka, R. F., & Cahn, J. W. (2004). Solid–liquid equilibrium for non-hydrostatic stress. *Acta Materialia*, *52*(6), 1663–1668. https://doi.org/10.1016/j.actamat.2003.12.010

Skelton, A. (2011). Flux rates for water and carbon during greenschist facies metamorphism. *Geology*, *39*(1), 43–46. https://doi.org/10.1130/g31328.1

Spiegelman, M. (1993). Physics of melt extraction: Theory, implications and applications. *Philosophical Transactions of the Royal Society of London Series A: Physical and Engineering Sciences*, *342*(1663), 23–41.

Stünitz, H., Thust, A., Heilbronner, R., Behrens, H., Kilian, R., Tarantola, A., & Fitz Gerald, J. D. (2017). Water redistribution in experimentally deformed natural milky quartz single crystals—Implications for H_2O-weakening processes. *Journal of Geophysical Research: Solid Earth*, *122*(2), 866–894. https://doi.org/10.1002/2016JB013533

Taetz, S., John, T., Bröcker, M., Spandler, C., & Stracke, A. (2018). Fast intraslab fluid-flow events linked to pulses of high pore fluid pressure at the subducted plate interface. *Earth and Planetary Science Letters*, *482*, 33–43. https://doi.org/10.1016/j.epsl.2017.10.044

Tajčmanová, L., Podladchikov, Y., Moulas, E., & Khakimova, L. (2021). The choice of a thermodynamic formulation dramatically affects modelled chemical zoning in minerals. *Scientific Reports*, *11*(1), 18740. https://doi.org/10.1038/s41598-021-97568-x

Tajčmanová, L., Vrijmoed, J., & Moulas, E. (2015). Grain-scale pressure variations in metamorphic rocks: Implications for the interpretation of petrographic observations. *Lithos*, *216–217*, 338–351. https://doi.org/10.1016/j.lithos.2015.01.006

Turcotte, D., & Schubert, G. (2014). *Geodynamics*. Cambridge University Press.

Ulmer, P., & Trommsdorff, V. (1995). Serpentine stability to mantle depths and subduction-related magmatism. *Science*, *268*(5212), 858–861. https://doi.org/10.1126/science.268.5212.858

van der Straaten, F., Schenk, V., John, T., & Gao, J. (2008). Blueschist-facies rehydration of eclogites (Tian Shan, NW-China): Implications for fluid–rock interaction in the subduction channel. *Chemical Geology*, *255*(1–2), 195–219. https://doi.org/10.1016/j.chemgeo.2008.06.037

Virieux, J. (1986). P-Sv-Wave propagation in heterogeneous media—Velocity-stress finite-difference method. *Geophysics*, *51*(4), 889–901. https://doi.org/10.1190/1.1442147

Vitale Brovarone, A., Butch, C. J., Ciappa, A., Cleaves, H. J., Elmaleh, A., Faccenda, M., et al. (2020). Let there be water: How hydration/dehydration reactions accompany key Earth and life processes. *American Mineralogist*, *105*(8), 1152–1160. https://doi.org/10.2138/am-2020-7380

Vrijmoed, J. C., & Podladchikov, Y. Y. (2022). Thermolab: A thermodynamics laboratory for nonlinear transport processes in open systems. *Geochemistry, Geophysics, Geosystems*, *23*(4), e2021GC010303. https://doi.org/10.1029/2021gc010303

Walther, J. V., & Orville, P. M. (1982). Volatile production and transport in regional metamorphism. *Contributions to Mineralogy and Petrology*, *79*(3), 252–257. https://doi.org/10.1007/bf00371516

Wang, L. H., Yarushina, V. M., Alkhimenkov, Y., & Podladchikov, Y. (2022). Physics-inspired pseudo-transient method and its application in modelling focused fluid flow with geological complexity. *Geophysical Journal International*, *229*(1), 1–20. https://doi.org/10.1093/gji/ggab426

Wayte, G. J., Worden, R. H., Rubie, D. C., & Droop, G. T. (1989). A TEM study of disequilibrium plagioclase breakdown at high pressure: The role of infiltrating fluid. *Contributions to Mineralogy and Petrology*, *101*(4), 426–437. https://doi.org/10.1007/bf00372216

Wheeler, J. (2014). Dramatic effects of stress on metamorphic reactions. *Geology*, *42*(8), 647–650. https://doi.org/10.1130/g35718.1

Wheeler, J. (2018). The effects of stress on reactions in the Earth: Sometimes rather mean, usually normal, always important. *Journal of Metamorphic Geology*, *36*(4), 439–461. https://doi.org/10.1111/jmg.12299

Wheeler, J. (2020). A unifying basis for the interplay of stress and chemical processes in the Earth: Support from diverse experiments. *Contributions to Mineralogy and Petrology*, *175*(12), 116. https://doi.org/10.1007/s00410-020-01750-9

Whitaker, S. (1969). Advances in theory of fluid motion in porous media. *Industrial & Engineering Chemistry*, *61*(12), 14–28. https://doi.org/10.1021/ie50720a004

Whitaker, S. (1986). Flow in porous media I: A theoretical derivation of Darcy's law. *Transport in Porous Media*, *1*, 3–25. https://doi.org/10.1007/bf01036523

Whitham, G. B. (1965). Non-linear dispersive waves. *Proceedings of the Royal Society of London. Series A. Mathematical and Physical Sciences*, *283*(1393), 238–261.

Xu, T., Apps, J. A., & Pruess, K. (2005). Mineral sequestration of carbon dioxide in a sandstone–shale system. *Chemical Geology*, *217*(3–4), 295–318. https://doi.org/10.1016/j.chemgeo.2004.12.015

Yarushina, V. M., Makhnenko, R. Y., Podladchikov, Y. Y., Wang, L. H., & Räss, L. (2021). Viscous Behavior of Clay-Rich rocks and its role in focused fluid flow. *Geochemistry, Geophysics, Geosystems*, *22*(10), e2021GC009949. https://doi.org/10.1029/2021gc009949

Yarushina, V. M., & Podladchikov, Y. Y. (2015). (De) compaction of porous viscoelastoplastic media: Model formulation. *Journal of Geophysical Research: Solid Earth*, *120*(6), 4146–4170. https://doi.org/10.1002/2014jb011258

Zheng, X., Cordonnier, B., McBeck, J., Boller, E., Jamtveit, B., Zhu, W., & Renard, F. (2019). Mixed-mode strain localization generated by hydration reaction at crustal conditions. *Journal of Geophysical Research: Solid Earth*, *124*(5), 4507–4522. https://doi.org/10.1029/2018JB017008